Physik Institut der Universität Zürich

– Bachelor Thesis –

Neutron Background Monitoring for XENON100

Enzio Crivelli

Supervisors: Prof. Dr. Laura Baudis
Dr. Marc Schumann
Dr. Teresa Marrodán Undagoitia

July 5, 2012

Abstract

The XENON100 experiment at the Laboratori Nationali del Gran Sasso (LNGS) in Italy is a direct dark matter detection experiment. A certain class of dark matter particles referred to as weakly interactive massive particles (WIMPs) shall be detected through scattering off Xe nuclei in a two-phase time projection chamber (TPC). The experiment provides several features for background elimination or discrimination. It is currently the most sensitive dark matter experiment featuring an extremely low absolute background.

One of the most crucial background components for XENON100 are neutrons since they can produce the same signal as a WIMP. Therefore it is interesting to measure the neutron flux in the close environment of XENON100 in order to improve the knowledge on this background. This thesis covers the design, installation and calibration of a small europium doped lithium-iodine (LiI(Eu)) neutron detector at XENON100 together with the measurement, data processing system and analysis methods to monitor the neutron background count rate. As a first step, the neutron detector shall measure relative neutron count rates to determine whether the neutron flux over the year is constant or fluctuates. The measurement data shall be compared to the expected neutron flux at LNGS followed by a brief overview listing possibilities for a better efficiency, purity and a better understanding of the detector.

Contents

1 Introduction

According to observations of structures much larger than the solar system, such as analyses of the cosmic microwave background, gravitational-lensing effects or rotation curves of galaxies, there is strong evidence that the energy content of the universe is made up of only $\sim$ 5% of ordinary baryonic matter, the elementary particles of planets, stars and ourselves. The remaining $\sim$ 95% can be separated into $\sim$ 72% dark energy which could be responsible for the observed accelerated expansion of the universe and $\sim$ 23% dark matter whose gravitation counteracts this expansion [1], [2], [3].

Although not yet detected directly, weakly interactive massive particles (WIMP's) have been established as one of the leading candidates among the classes of dark matter particles. They arise in many extensions of the standard model like Supersymmetry or Universal Extra Dimensions. They should be distributed in dark halos around galaxies such as the Milky Way, allowing for their direct detection via weak interactions in terrestrial detectors [4], [5] (and references therein).

The XENON100 experiment at the INFN Laboratori Nazionali del Gran Sasso (LNGS) in Italy is designed to search for WIMPs, i.e. it aims to directly detect them through elastic scattering off the target Xe-nuclei which are present mainly in liquid form in a two-phase liquid-gas time projection chamber (TPC) [5]. Its design allows for the measurement of the recoil energy and the three spatial coordinates of each event occuring in the liquid Xe target with millimeter resolution.

The characteristics of the expected WIMP signal makes the detection extremely challenging for every direct detection experiment. The predicted event rate is very small due to the tiny interaction cross section. It might be one event per ton of interaction material and per year or even less. Moreover, the signal of the standard WIMP scenario is expected to occur at very low nuclear recoil energies of the order of a few keV. Therefore a low energy threshold and an extraordinary low radioactive background must be achieved. Hence the location of XENON is deep underground at the INFN LNGS (see Fig.1.1), to avoid cosmic radiation [5] (and references therein).

The two-phase TPC of XENON allows the detection of two small signals S1 and S2 originating from an interaction with a Xe nucleus. The prompt light signal S1 from Xe scintillation is detected by two arrays of photomultipliers. The secondary scintillation light signal S2 arises in the Xe gas phase. This process leads to the ionization of Xe atoms which are separated from the Xe ions and drifted upwards through the liquid Xe by a strong electric field and extracted into the gas phase. S2 is the ionization signal, delayed with respect to S1 by the electron drift time. It is detected with the same photomultiplier arrays. The ratio S2/S1 produced by a WIMP (or nuclear) recoil is different from that produced by an electronic recoil allowing a high gamma and beta particle background rejection [5] (and references therein).

The TPC's precise event localisation together with the self-shielding capability of the liquid Xe allows background suppression by fiducial volume cuts. Moreover the detector is surrounded by a shield consisting of copper, polyethylene, lead and water (from inside out) to reduce the background from gamma and neutron radiation. A very low intrinsic

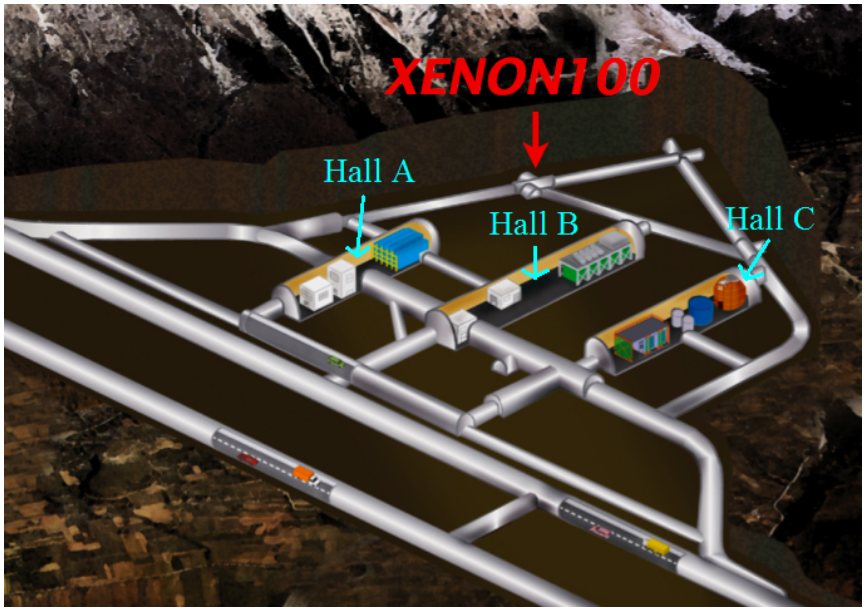

Figure 1.1: Location of the XENON100 Experiment underground at LNGS [6], [7].

background is achieved through the careful selection of the detector materials to have extraordinary radiopurity. These were screened by a 2.2 kg high-purity Ge detector in an ultra-low background environment operated at LNGS as well as by the LNGS screening facilities. Together with Monte Carlo simulations for internal and external background an overall background model was constructed [5].

The most crucial background component in XENON are neutrons since they also scatter elastically on Xe nuclei. They can produce the exact same signal as a WIMP wherefore a discrimination of WIMPs from neutrons is not possible. Hence it is interesting to measure the neutron flux in the environment of XENON100 in order to constantly monitor this background component.

As a first step a simple neutron detector shall be installed in the XENON100 environment measuring relative neutron rates to determine whether the neutron rate over the year is constant or fluctuating. The results shall be compared to the expected neutron flux at LNGS to reveal improvement potential [13]. This thesis covers the design of the detection system, its calibration and the analysis methods to achieve this objective.

The results/methods might be of further use for experiments which try to detect WIMPs by an annual modulation. Since the Dark Matter is expected to be distributed in halos around the Milky Way, the flux of dark matter particles should fluctuate over the year as the earth revolves around the sun (see Fig.1.2). The fluctuating WIMP flux would become observable in a suitable detector. For this detection method it is crucial to eliminate a fluctuation of the background, including the neutron flux. For example the DAMA experiment uses the annual modulation method. It is an experiment which has reported a positive signal since several years [9] (and references therein).

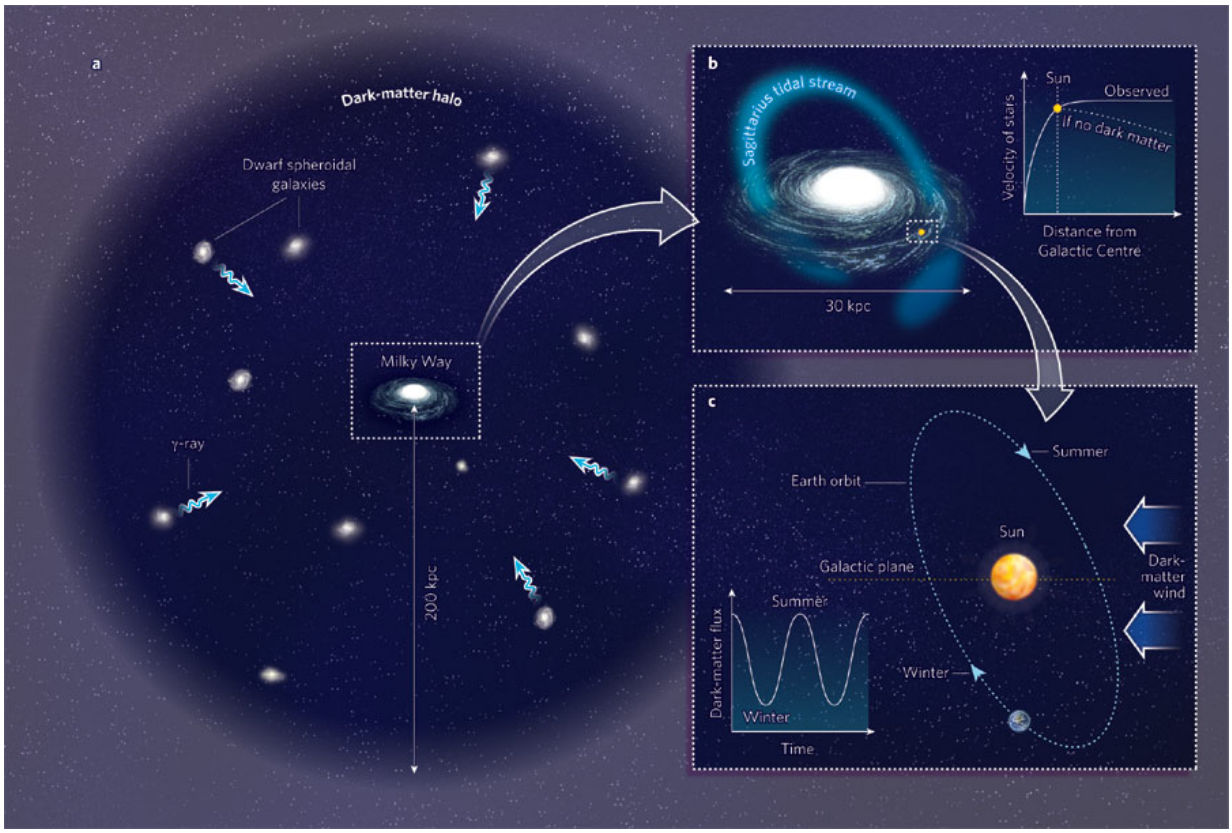

Figure 1.2: a), b) The rotational velocity of its stars and gas indicates that the Milky Way is embedded in a dark matter halo extending out to a radius of about 200 kiloparsecs (kpc). High-energy rays may be produced by the annihilation of dark matter particles in neighbouring dwarf spheroidal galaxies and near the galactic centre, where the dark matter density is expected to be the highest. The dark-matter density may also be enhanced in the tidal stream of matter that trails from the Sagittarius dwarf galaxy and entangles the Milky Way.
c) The Earth's orbit through the galactic dark-matter halo may produce a modulation of the dark-matter flux identified in experiments that aim to detect dark matter directly. A smaller flux is expected when the Earth moves in the same direction as the dark matter "wind" from the galactic halo (in winter) than when it moves against it (in summer) [8].

2 Production and Interaction of Neutrons

In order to design measurement systems for the detection of neutron background, fundamental principles of particle interactions in matter have to be known since they are the basis of all current particle detection devices and thus determine the primary design possibilities of a measurement setup.

The main processes involved in the experiment can be categorized into two groups: the production of neutrons and their interaction with matter. More information about particle production and interaction is presented in Appendix: Particle Interaction in Matter and in more detail in [10].

2.1 Production of Neutrons

Commercially available neutron sources, as used in this experiment for calibration purposes, are either based on spontaneous fission or a nuclear reaction. Natural neutron emitters which can be used practically in the lab do not exist. They have to be produced synthetically. The more convenient method of producing neutrons is with the nuclear reactions (α, n) or (γ, n).

For the calibration of this experiment (see chapter 3.3.2), a ^{241}Am^{9}Be neutron source is used. Such a source is generally made by mixing the target material ^{9}Be with a suitably strong α- or γ-emitter. In this case the α-emitter ^{241}Am is fixed onto one flat side of the cylindrical ^{9}Be target [12]. Under α bombardment ^{9}Be undergoes the following reactions which lead to the production of free neutrons:

$$\alpha \; + \; {}^{9}Be \; \longrightarrow \; {}^{13}C^{(*)} \; \longrightarrow \; \begin{cases} {}^{12}C^{(*)} \; + \; n \\ {}^{8}Be \; + \; \alpha \; + \; n \quad [10] \; . \\ 3\alpha \; + \; n \end{cases} \tag{2.1}$$

The dominant reaction is the decay from ^{13}C to ^{12}C or to the 4.44 MeV excited state of ^{12}C which is denoted by $^{(*)}$. A neutron yield of about 70 n's per 10^6 α's is obtained if ^{241}Am is the α-source. The α-emitter's half-life and activity determines therefore the half-life and activity of the neutron production.

For incident α's of a fixed energy the energy spectrum of the emitted neutrons should theoretically show monoenergetic lines corresponding to the different transitions which are made. In mixed sources such as AmBe however there is a smearing of the α-particle spectrum due to the energy loss between origin and capture of the α-particle inside the source and target material itself such that a large smearing in neutron energy results. This is illustrated in Fig.5.6b.

If ^{241}Am decays by emitting an α-particle into ^{237}Np this daughter nucleus offers many possibilities of excited states whose de-excitation into the ground state results in the emission of γ-particles. The nuclear level diagram of ^{241}Am is therefore quite complex and it makes sense to simplify it by taking into account only branching ratios larger than 0.3% shown in Fig.5.6a.

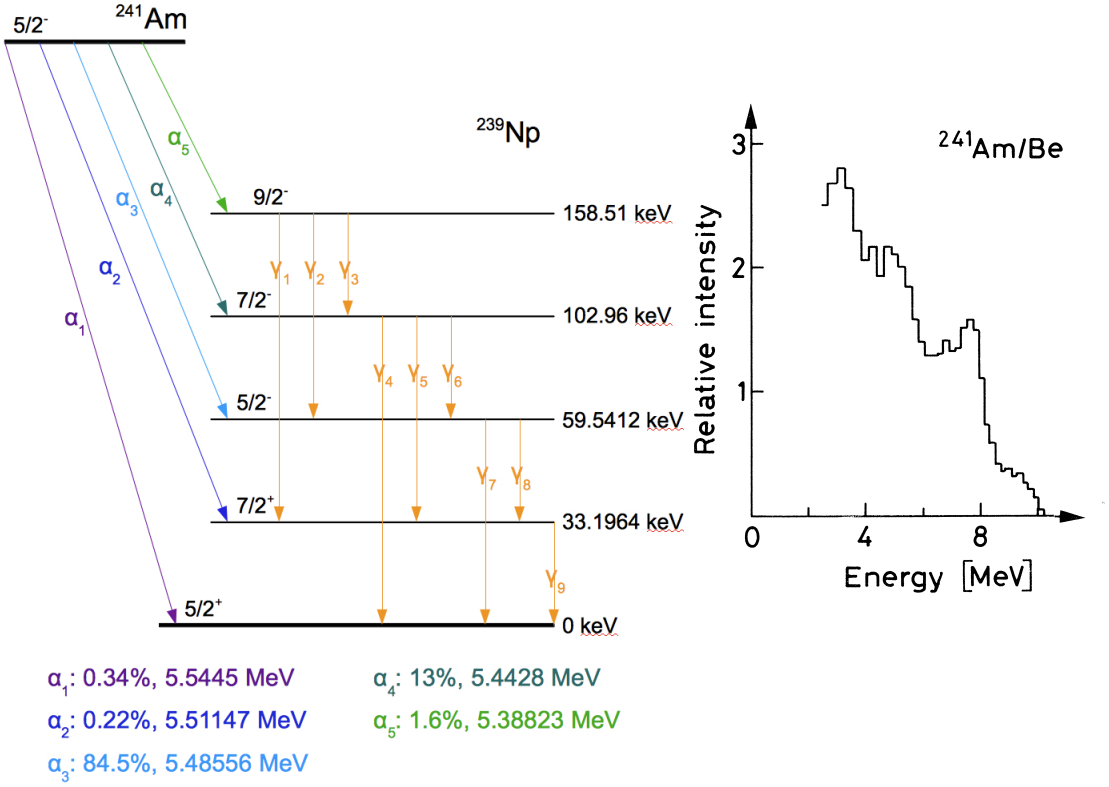

Figure 2.1: a) Nuclear level diagram of ^{241}Am restricting the α-decay possibilities to branching ratios larger than 0.3% [11].
b) Neutron energy spectrum from ^{241}Am^{9}Be [10].

2.2 Interactions of Neutrons; Moderation and Capturing

As the photon, the neutron does not possess an electric charge. It is not subject to electromagnetic interactions with the electrons and nuclei in matter. Instead, its principal way of interaction is through the strong force with nuclei whereat the interaction probability is much rarer compared to the one of electrons for instance due to the short range of this force. A neutron must come within $\simeq$ 1 fm of the nucleus before an interaction can take place. Since baryonic matter is mainly "empty space" the neutron is a very penetrating particle, much more than γ-rays. When a neutron interacts, it may undergo a variety of nuclear processes depending on its energy:

1. a) Elastic scattering from nuclei, i.e. $A(n,n)A$.
   This process is the principal mechanism of energy loss of neutrons with energies of about a few MeV.

b) Inelastic scattering, e.g. $A(n,n')A^{(*)}$, $A(n,2n')B$, etc.
After such reactions the nucleus is left in an excited state which might later decay via another form of radiative emission like γ-rays. The neutron must have sufficient energy to excite the nucleus, usually of the order of 1 MeV or more, for the inelastic reaction to occur. Below this threshold only elastic scattering occurs.

2. a) Radiative neutron capture, i.e. $n + (Z,A) \rightarrow \gamma + (Z, A+1)$.
In general the cross section for neutron capture goes like

$$\sigma \simeq \frac{1}{v}, \tag{2.2}$$

where v is the velocity of the neutron. The capture is therefore most likely at low energies. Resonance peaks superimposed upon this dependence may also be present depending on the element. At these energies the capture probability is greatly enhanced.

b) Other nuclear reactions such as (n,p), (n,d) [1], (n,α), (n,t) [2], $(n,\alpha{+}p)$, in which the neutron is captured and charged particles are emitted. These reactions occur generally in the eV to keV region. The capture cross section and resoncances follow the same behaviour as for radiative neutron capture.

c) Fission, i.e. (n,f) [3], which again is most likely at low energies.

3. High-energy hadron shower production which occurs only for very high-energy neutrons with $E_n > 100$ MeV.

Neutrons are classified according to their energy since their interactions depend strongly on their energy, although no strict boundaries exist among the classes. High-energy neutrons have energies above $E_n \simeq 100$ MeV, those between a few ten's of MeV and a few hundred keV are known as fast neutrons. Between $E_n \simeq 100$ keV and $E_n \simeq 0.1$ eV, where nuclear resonance reactions occur, neutrons are referred to as epithermal, whereas at lower energies comparable to the thermal energy at room temperature, i.e.
$E_n \simeq kT \simeq 1/40$ eV $= 25$ meV, neutrons are called thermal. Moreover for energies lower than the thermal, neutrons are referred to as cold where $E_n \lesssim 2$ meV, and below as ultracold where $E_n \lesssim 0.2$ meV.

The total probability for a neutron to interact with matter is given by sum of the indivitual cross sections:

$$\sigma_{\text{tot}} = \sigma_{\text{elastic}} + \sigma_{\text{inelastic}} + \sigma_{\text{capture}} + ... \tag{2.3}$$

[1] d denotes deuterium which is the isotope ${}^2_1\text{H}$ (without electrons)
[2] t denotes tritium, the isotope ${}^3_1\text{H}$
[3] f denotes one ore more decay nuclei along with one or more neutrons

The slowing down of neutrons by interaction in matter is called moderation. If a fast neutron enters into matter, it scatters back and forth on the nuclei, elastically and inelastically. It loses its kinetic energy until it comes into thermal equilibrium with the surrounding atoms. At this point it will diffuse through matter until it is finally captured by a nucleus and undergoes one of the processes mentioned above (2.a), b), c)). The neutron may also undergo a nuclear reaction or be captured before attaining thermal energies, especially if resonances are present. However the energy dependence of the cross-section in eq.(5.17) favors the survival of the neutrons down to thermal energies.

Elastic scattering (1.a)) is the principal mechanism of energy loss for fast neutrons. At energies of several MeV, which is the case in this experiment, the problem can be treated nonrelativistically with conservation laws. The calculation yield energy range limits for the scattered neutron:

$$\left(\frac{A-1}{A+1}\right)^2 E_{\text{neutr.}} < E'_{\text{neutr.}} < E_{\text{neutr.}} \tag{2.4}$$

where the limits correspond to $\cos(\theta_{cm}) = \pm 1$ and θ_{cm} is the scattering angle in the cm-frame (see Fig.2.2). In the case of scattering at protons, $A = 1$ and

$$0 < E'_{\text{neutr.}} < E_{\text{neutr.}}. \tag{2.5}$$

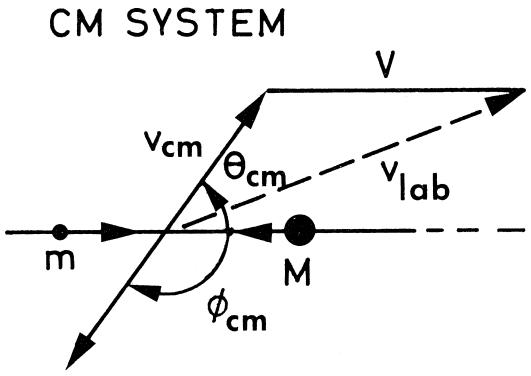

Figure 2.2: Elastic scattering of a neutron on a nucleus of mass M in the center of mass (cm) frame [10].

Therefore the slowing down of neutrons is most efficient when protons or light nuclei are used. This is not surprising since intuitively, the lighter the nucleus, i.e. the smaller the mass difference between neutron and target particle is, the more recoil energy it absorbs from the neutron. This explains the use of hydrogenous materials such as water (H_2O), paraffin ($(CH_2)_n$) and polyethylene ($(C_2H_4)_n$) for neutron moderation.

The energy distribution of the scattered neutron at not too high energies, i.e. $E_{\text{neutr.}} \leq 15$ MeV, is given by probability density functions shown in Fig.5.8. It illustrates the complexity of energy information of neutrons during scattering: the function as well as the energy limits are dependent on the number of scatterings. In fact the treatment is

even more complicated if the calculation is not restricted to an upper limit on the incident neutron energy as well as to the approach of s-wave scattering. Moreover an exact result would need the number of scatterings which is in general highly material dependent and only calculable as an average due to the statistical distributed variation in the path lengths between the scatterings.

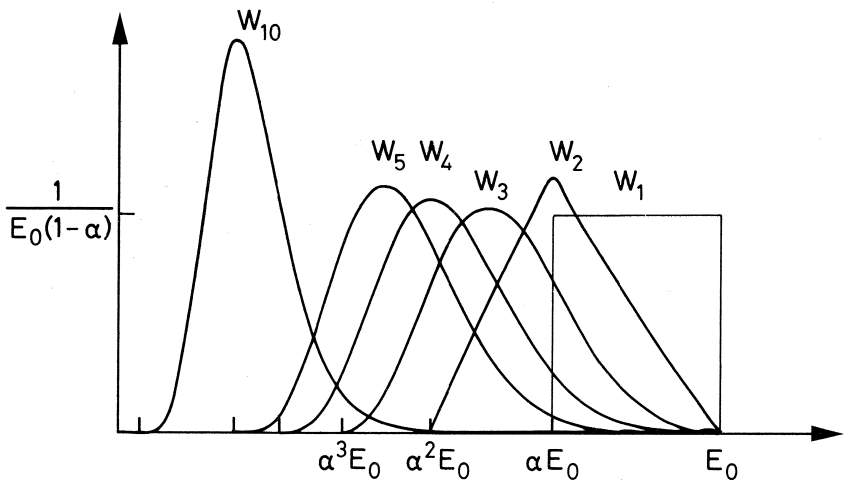

Figure 2.3: The energy distribution of neutrons after one resp. several elastic scatterings. It shows the probability density function w versus the scattered neutron energy $E'_{\text{neutr.}}$ within the boundaries $0 < E'_{\text{neutr.}} < E_{\text{neutr.}}$ developing with the number of elastic scatterings where $\alpha = \left(\frac{A-1}{A+1}\right)^2$ and A is the atomic mass number. I.e. w_1 is the distribution after one scattering, w_2 after two, etc. [10].

3 Experimental Setup and Calibration

All particle physics detectors are based on the same fundamental principle: the transfer of a part or all of the radiation energy to the detector material where it is converted into some other form more accessible to human perception. As seen in chapter 2, neutron radiation must first undergo some sort of reaction inside the detector which produces charged particles which in turn ionize or excite the detector atoms. The form in which the converted energy appears depends on the detector and its design. In scintillation detectors, for example, both the excitation and ionization include molecular transitions which result in the emission of light.

Those are essentially electrical in nature, i.e. the light information from the detector is transformed by use of a light sensor into electrical impulses which can be treated by electronic means. This takes advantage of electronics and computers to provide a faster and more accurate treatment of the information. Indeed the detector used in this experiment for the detection of neutrons can not be exploited otherwise. Therefore when discussing "the detector" the electronics is meaned as well.

Hence chapter 3.1 gives an overview of the whole measurement system whereas chapter 3.2 explains the system components along with its purposes.

In order to produce analyzable information the components of the detector have to be adapted to each other. Moreover a calibration is necessary such that the neutron signal can be identified. Chapter 3.3 describes the procedures which enable the detection of neutrons at the XENON100 experiment at LNGS, Italy.

3.1 Experimental Overview

The final measurement setup shown in Fig.3.1a consists of 3 main components, LiI(Eu) neutron detector, data acquisition system (electronics) and moderator which are assembled together in the plastics box. The data acquisition system consists of commercially available parts. The LiI(Eu) detector is also commercially available whereas the moderator is designed especially for the neutron thermalization for this detector. This polyethylene moderator encloses the LiI(Eu) detector except for its back side where the high voltage and signal connection is.

In the ideal case an incident neutron will slow down inside the polyethylene until it reaches thermal energies and is captured by a Li-atom of the detector. By the nuclear reaction (3.1) an α- and a ^{3}H-particle are created with a combined initial kinetic energy of 4.78 MeV [13], [14], [15], [16]. Those particles are subsequently slowed down by collisions with electrons of the surrounding atoms which in turn are ionized or brought into excited states. The de-excitation leads to the emission of scintillation light which is converted to an electrical signal by the PMT of the detector. This output is then amplified and shaped into semi-gaussian form by the high voltage and amplification module, which produces also the high operation voltage needed by the detector, and digitized by the multi channel analyser (MCA).

A laptop runs the data acquisition program, which is fed by data from the MCA via an

USB connection, and moreover serves as the data saving platform. It is connected to the LNGS internal LAN and WAN network by an ethernet connection enabling the distribution of the data for its analysis. Fig.3.1b gives the schematical overview of these mentioned processing steps.

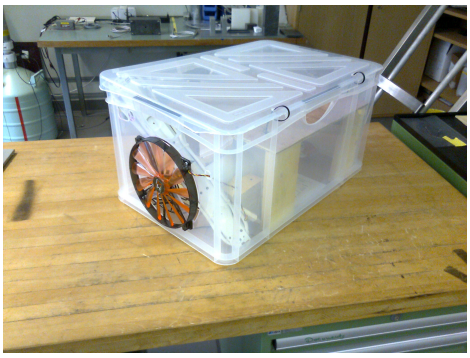

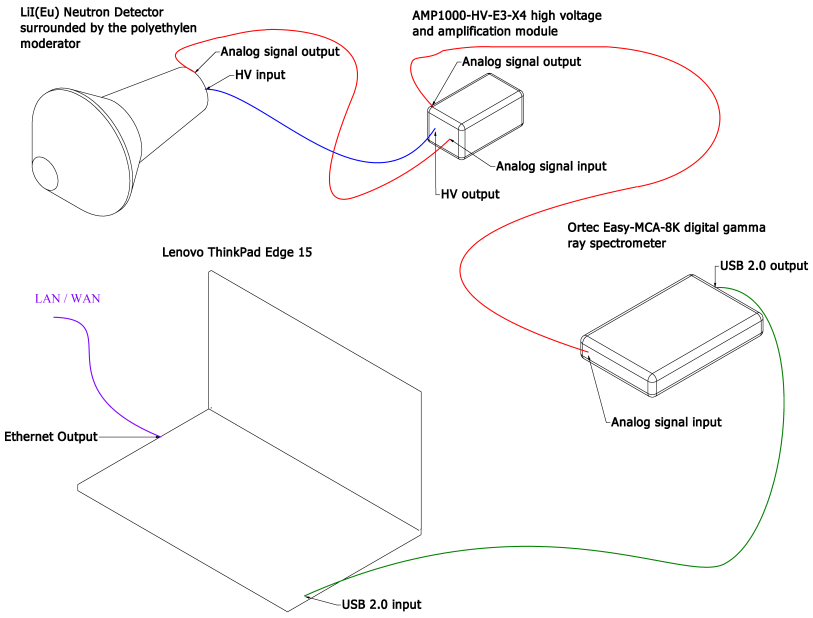

Figure 3.1: Overview of the final measurement setup:
a) Picture of the plastics box containing the LiI(Eu) detector, moderator and associated electronics
b) Schematic illustration of the high voltage, signal and data flow between its processing modules; red: Detector signal (clockwise), blue: Detector Operation voltage (counterclockwise), green: Digitized detector signal (clockwise), violet: Ethernet access for data analysis (clockwise).

Of course not every incident neutron will thermalize completely. Some of them may not even reach the moderator due to scattering at the plastic walls of the box of about 3 mm thickness or at the electronic components of the detector system (e.g PMT, laptop, etc.) residing in the direct neighborhood of the moderator. However not much incident neutrons are lost this way since the electronics does not consist of material of a low atomic number, in particular ^{1}H, and all the plastic surfaces (hydrogenous material) are thin. Therefore the neutron loss resp. moderation contribution of all the components of the detection system surrounding the moderator can be neglected.

If a neutron reaches the moderator, it will be slowed down by elastic scattering mainly on the protons of the polyethylene. It scatters back and forth through the material until it reaches the same average energy as the surrounding atoms and is thus thermal. From that point on it only diffuses slowly through the material. At every scatter and during the diffusion its propagation direction will change and will remain unknown due to the large amount of scatterings, the unknown scattering angle itself and the unknown incident

direction. The only valid statement is that the incident direction of the neutrons before the moderation is distributed isotropically. Therefore it is possible that such a neutron leaves the polyethylene during the moderation process before it can be captured by the LiI(Eu) detector. The amount of neutrons lost this way is a priori unknown as well.

When the thermalized neutrons reach the detector they are captured by ^{6}Li with the large cross section of $\approx$ 940 b [14], [15], [16]. Due to the design of the moderator surrounding the LiI(Eu) detector, the neutron is not always thermal but can possess more energy. Therefore its caption is less likely and the cross section lower. Moreover a probability exists that it might not be captured. Thus a few neutrons will also be lost due to this effect.

3.2 Final Measurement Setup

The three main components of the setup, i.e. LiI(Eu) detector, moderator and the associated data acquisition system are presented here in more detail together with the transformation processes between incident neutron and resulting measurement data. The setup is schematically listed in Fig.3.1b.

3.2.1 Neutron Detector

The chosen LiI(Eu) detector Scionix 25.4B3/1.5-ME1-Li shown in Fig.3.2a is designed to detect neutrons indirectly over the nuclear reaction

$$^6_3\mathrm{Li} + n \rightarrow {}^7_3\mathrm{Li}^{(*)} \rightarrow {}^3_1\mathrm{H} + \alpha. \qquad \text{[10], [13], [14], [15], [16]} \tag{3.1}$$

The dimensions and components of the LiI(Eu) detector with their alignment are illustrated schematically in Fig.3.3. The cylindric crystal has a radius of 12.7 mm and a height of 3 mm whereas the PMT has a radius of 18.825 mm (1.5/2 in) [18].

If an incident thermal neutron hits a ^{6}Li nucleus of the LiI(Eu) crystal, the reaction (3.1) leads to the decay of the ^{7}Li and the emission of a ^{3}H and α-particle with a Q-value of $Q = 4.78$ MeV. This energy is kinematically split between the decay products inversely proportional to their masses. The ^{3}H receives $E_{^3H} = 4/7 \cdot Q = 2.73$ MeV and the α-particle $E_\alpha = 3/7 \cdot Q = 2.05$ MeV [13], [14], [15], [16].

The ^{3}H- and α-particles lose subsequently their energy due to inelastic collisions with electrons of the surrounding atoms which are ionized or taken into excited states (see ch. 5.5). Due to the the electronic band structure of the crystal (see in Fig.3.4a), the ionization electrons are lifted up from the valence band into the conduction band of the crystal creating a free electron and a free hole.

The doped ^{153}Eu atoms serve as impurity atoms which create electronic levels in the otherwise forbidden energy gap between valence- and conduction band. A migrating hole encountering such an impurity can ionize the impurity atom. A subsequent arriving electron can "fall" into the hole and make a transition back to the valence band emitting a photon of a characteristic wavelength.

In case of excitation, the electron is lifted into a band (the exciton band) located just below the conduction band creating a bound electron hole pair which can move freely

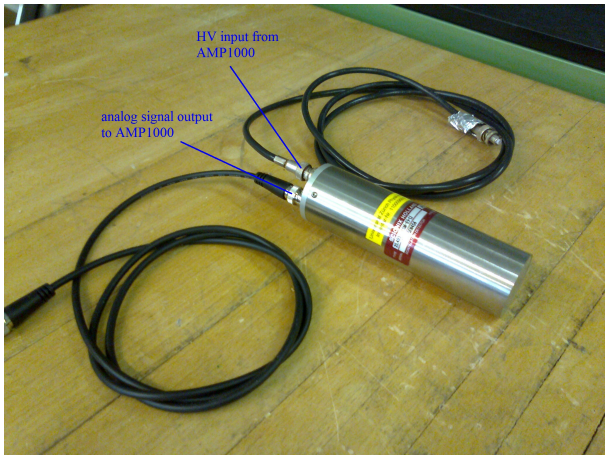

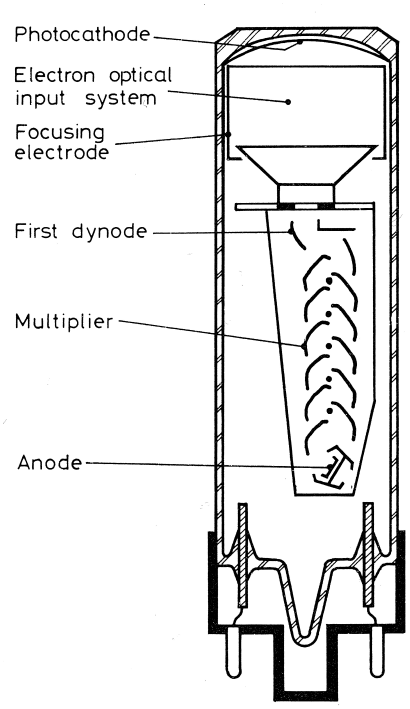

Figure 3.2: a) Picture of the LiI(Eu) detector with cables for high voltage supply and signal read out.
b) Schematic illustration of a photomultipier tube (PMT) using a linear focused dynode array [10].

through the crystal. Just like before the hole can ionize the impurity atom and the bound electron falls into the opening and performs a transition back to the valence band emitting again a photon of characteristic wavelength. These photons are referred to as scintillation light.

The time evolution of the light emission process is generally described by an exponential decay. However not every photon is emitted promptly within 10^{-8} s for most scintillators [1]. In that case the emission is delayed because excited states can be metastable resulting in an afterglow. The delay time may last from a few microseconds to hours depending on the material [10]. For such a process a more accurate description of the time evolution is given by a two-component exponential decay consisting of a fast and a delayed exponential term shown in Fig.3.4b.

For LiI(Eu) the effective average decay time has a decay constant of $\tau_f = 1.2$ μs which is about two times larger compared to other inorganic scintillation crystals and about a factor of 10^3 larger compared to plastic scintillators [10].

Due to the band structure of LiI(Eu) the photon emission is not monoenergetic. The emission spectrum has its maximum at a wavelength of $\lambda_{\text{max}} = 475$ nm [10].

The number of photons emitted, i.e. the light output is about a factor of 3 lower

[1] 10^{-8} s is roughly the time taken for atomic transitions

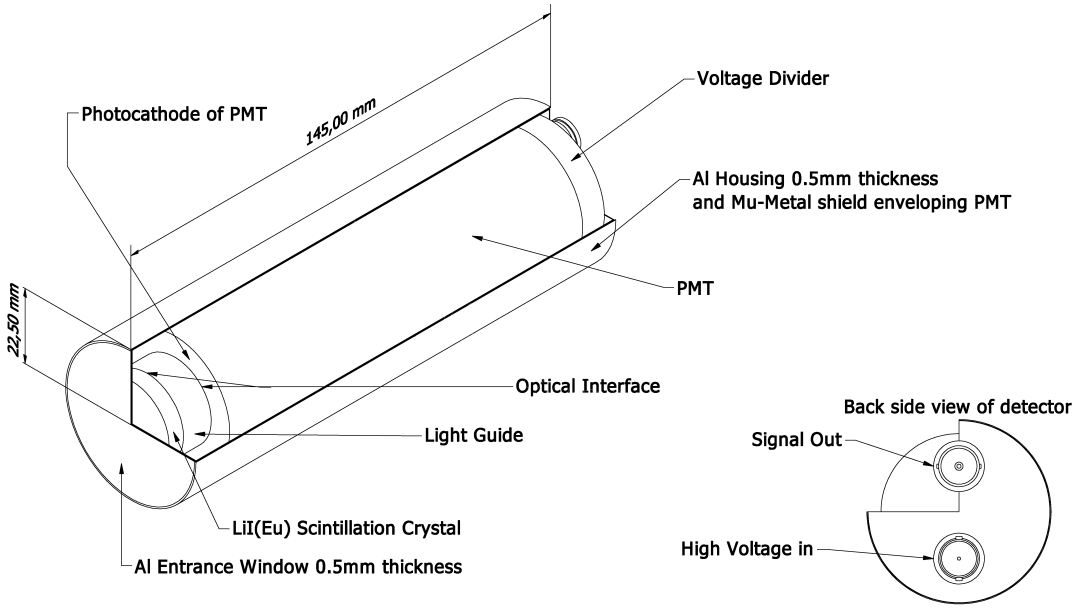

Figure 3.3: Schematic drawing of the LiI(Eu) detector components [18].

compared to other inorganic crystal scintillators, a bit higher than for plastic and liquid scintillators, and 75% of the one of anthracene, the organic crystal scintillator with the highest light output [10]. Strictly speaking this quantity is not proportional to the energy deposited by the ionizing α- and ^{3}H particles. In reality it is a complex function dependent of the particle and its specific ionization resp. excitation and energy. However for heavy particles with energies above 1 MeV the deviation from linearity is small such that linearity can be assumed in good approximation.

A portion of the nonlinearity can be explained by quenching interactions between the excited atoms resp. molecules created along the path of the incident particle. These interactions drain some energy which would otherwise lead to the production of scintillation light [2].

The light output is also temperature dependent. However this dependence is weak at room temperatures and variations in the light output can be eliminated if the temperature is maintained constant.

The LiI(Eu) crystal is transparent to the emitted photon spectrum with a refractive index of $n = 1.955$ [10]. Hence photon self-absorption by the scintillation material is small especially for small crystal volumes as it is the case here. The scintillation light is transmitted to the photocathode of the photomultiplier tube (PMT) coupled to the crystal via a light guide. The coupling between the scintillator and the PMT must be made such

[2] In general two types of quenching occur, the chemical and optical. In the former energy is transferred onto an atom resp. molecule which is not able to emit photons. In the latter an already emitted photon is self-absorbed by an atom resp. molecule of the scintillator. Its energy is converted into further photon emission of the same or different energy or other processes like thermal excitation. Either way the photon energy spectrum is shifted downwards to lower energies.

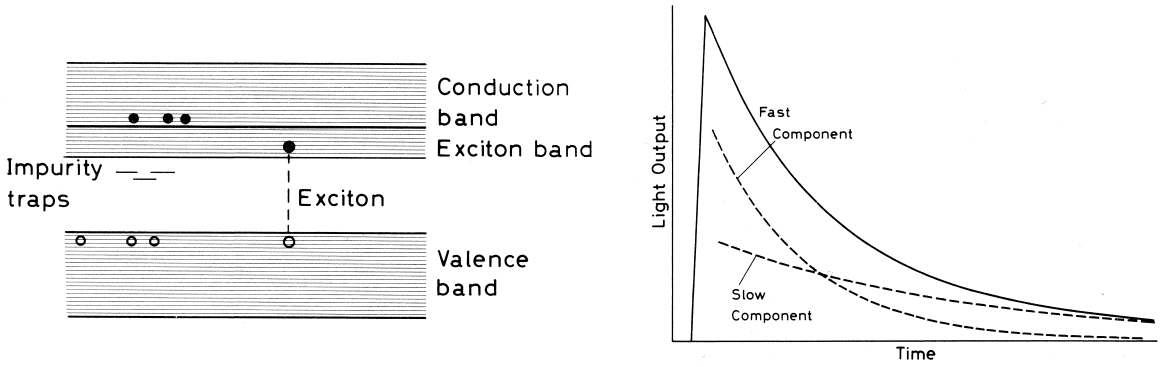

Figure 3.4: a) Electronic band structure of inorganic crystals. Besides the formation of free elecrons and holes loosely coupled electron-hole pairs (excitons) are formed. They can migrate through the crystal and be captured by impurity centers. In LiI(Eu) crystals these traps are formed by the activator ^{153}Eu [10].
b) Shape of the light output as a function of time. It consists of a slow and fast exponential component. The solid line represents the over-all light curve [10].

that it allows a maximum of light transmission. The optical contact between the two media is therefore made of a material whose index of refraction is as close as possible to those of the scintillator crystal and the PMT photocathode window. In order to redirect the otherwise escaping scintillation light back into the crystal or light guide internal reflexion is used. The refractive index is an advantage since it allows a relatively large total reflexion angle compared to other scintillators such that the light can be efficiently collected by the photocathode.

Due to the hygroscopicity of LiI the crystal must be protected from the moisture in the air by housing it in an air tight enclosure.

Fig.3.2b shows a schematic diagram of a PMT. It consists of the photocathode followed by an electron collection system, an electron multiplier section or dynode chain and finally an anode from which the final signal for further processing is taken. During operation a high voltage is applied to the cathode and dynodes such that a potential ladder is set up along the cathode - dynode - anode structure.

When an incident photon hits the photocathode an electron is emitted via the photoelectric effect. The electric field due to the potential difference then accelerates the electron towards the first dynode. When it impinges, it transfers some of its energy to the electrons in the dynode. This causes the emission of secondary electrons which in turn are accelerated towards the next dynode where more electrons are released and accelerated. Therefore an electron cascade along the dynode chain is created which is collected at the anode giving a measurable current. The PMT used for the LiI(Eu) detector contains 12 dynode stages whereby a typical electron gain of the order of 10^6 is obtained [10], [18].

The efficiency for the photoelectric conversion in the photocathode, the quantum effi-

ciency

$$\eta(\lambda) = \frac{\text{number of photoelectrons released}}{\text{number of incident photons on cathode}(\lambda)} \qquad [10] \quad , \tag{3.2}$$

is strongly dependent of the wavelength of the incident light and the structure of the material. For the bialkali photocathode used here, the maximal quantum efficiency is $\eta_{\max} = 26\%$ for a wavelength λ a bit below $\lambda_{\max}$ of LiI(Eu). The spectral range of the photoemission spectrum of the crystal and the spectral response range of the quantum efficiency are reasonably consistent, i.e. the wavelength corresponding to the maximum of the photoemission spectrum matches a quantum efficiency of $\eta(\lambda_{\max}) \approx 20\%$ [10].

It is crucial to have a stable voltage applied to the dynodes. Assuming the applied voltage is equally divided among 10 dynode stages, a 1% change in supply voltage results in a 10% variation in the electron gain. To maintain a gain stability of 1% the voltage must be therefore kept within 0.1% [10]. In order to achieve this a high voltage supply, situated in the high voltage and amplification module, in conjunction with a voltage divider directly interconnected to the PMT is used. This divider consists of a chain of resistances chosen such that they provide the desired voltage to each of the dynodes.

If the temperature and the applied voltage are kept constant, the electron gain is not only reasonably stable but also the charge pulse signal at the anode is proportional to the initial number of electrons emitted by the photocathode. In addition the number of incident photons hitting the photocathode is of course proportional to the initial number of electrons due to the scaling property of the quantum efficiency. Hence the charge pulse is proportional to the energy deposition of the α or ^{3}H due to the approximate linear behaviour of the light output with respect to the α or ^{3}H energy deposition.

Therefore the detector is in principle capable of providing information about the energy deposited by the two particles. However energy information about neutrons is not possible to achieve since reaction (3.1) holds for arbitrary neutron energies, i.e. a neutron capture always yields the same Q-value. This is in particular the case in this experiment where the incident neutron energy is influenced by moderation to increase the capture efficiency.

The high capture cross section of ^{6}Li of $\sigma \approx 940$ b for thermal neutrons is the reason for combining the base material iodine with Li. It is enriched to a high extent of $\approx 90\%$ with ^{6}Li to maximize the intrinsic efficiency of the crystal [13], [14], [15], [16], [17]. A neutron may also be captured when it has a higher than the thermal energy. The $1/v$ dependence of the cross section (see chapter 2.4) ensures that the cross section drops not drastically for neutron energies close enough to the thermal energy.

Due to the short reach of the ^{3}H and α-particles in matter it can be assumed that all of them are fully stopped inside the LiI(Eu) and hence deposit all their kinetic energy inside the crystal. (E.g. a 10 MeV proton loses all of its kinetic energy in 0.25 mm of copper whose density is about twice the one of LiI(Eu) [10].)

Other radiation types than ^{3}H or α-particles, for example γ-radiation, can also ionize or excite the atomic electrons of the crystal. This radiation is the main background component but becomes useful in the detector calibration (see chapter 3.3.1).

3.2.2 Polyethylene Moderator

As briefly mentioned above a moderator is desired to thermalize neutrons to increase the neutron capture efficiency. Since the capture cross section is the highest for thermal neutron energies, so is the capture efficiency which drops with a $1/v$ dependence.

Since incident neutrons enter the LiI(Eu) detector from arbitrary directions the moderator has to surround the cylindrical detector and moderate the neutrons in the same way from all directions such that they are thermalized at the surface of the scintillation crystal. This is the ideal model providing the foundation on which the shape of the moderator is based on.

The theory of neutron moderation (chapter 2.2) concludes that basically the more hydrogen the material contains per unit volume the less material is needed for the neutron thermalization. Hence the right moderator material should have a high hydrogen ratio, a high density and be easy available and to handle. These requirements result in the choice of polyethylene ($(C_2H_4)_n$).

The ideal shape of the moderator along the detector axis is calculated analytically using trigonometry and is shown in Fig.3.5a. Some minor simplifications have to be made to avoid a large complexity of the calculation: Neutrons which incide on the orange or green part of the moderator in Fig.3.5a are thermalized not on the front surface (for orange part) resp. back surface (for green part) of the crystal but in their centers.

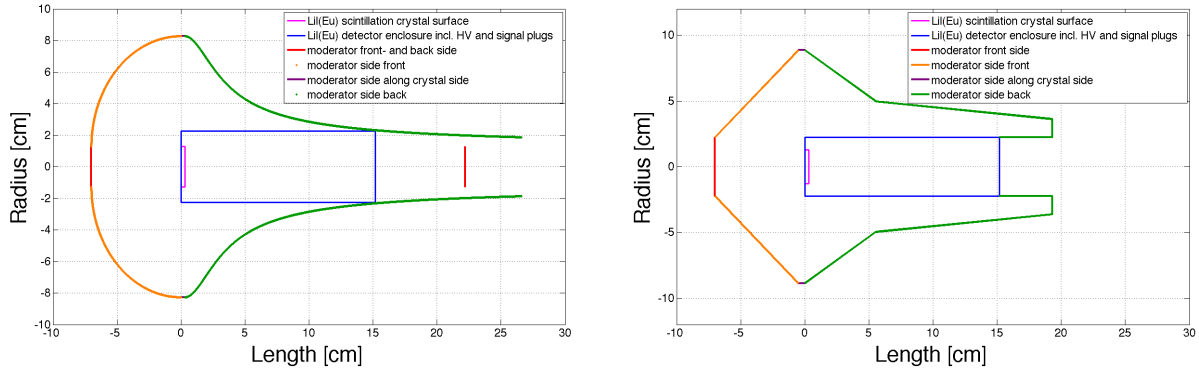

Figure 3.5: Schematical illustration the moderator shape. The idea is that incident neutrons entering the LiI(Eu) crystal have been thermalized by the polyethylene moderator in the same way from all directions in order to maximize the neutron capture efficiency. The development of the final form of the moderator is done in two steps:
a) The shape resulting from the ideal approach using only small simplifications.
b) The final shape after applying all simplifications.

As mentioned in chapter 3.1 the moderation contribution of all the components of the detection system surrounding the moderator can be neglected.

In chapter 3.3 the polyethylene thickness for maximal efficiency is determined by measurements with a $^{241}Am^{9}Be$ neutron source to be $d_{PE} = 7$ cm. Its variation can be 1 cm without reducing the efficiency by more than 5% (see Fig.3.12a).

This together with Fig.3.5a indicate that further simplifications of the moderator shape are reasonable such that it can be fabricated with a resonable amount of work. The basic simplification concept is to substitute all curves by straight lines. The resulting final shape of the moderator after applying all simplifications is shown in Fig.3.5b and Fig.3.6 which shows a schematical drawing including the dimensions.

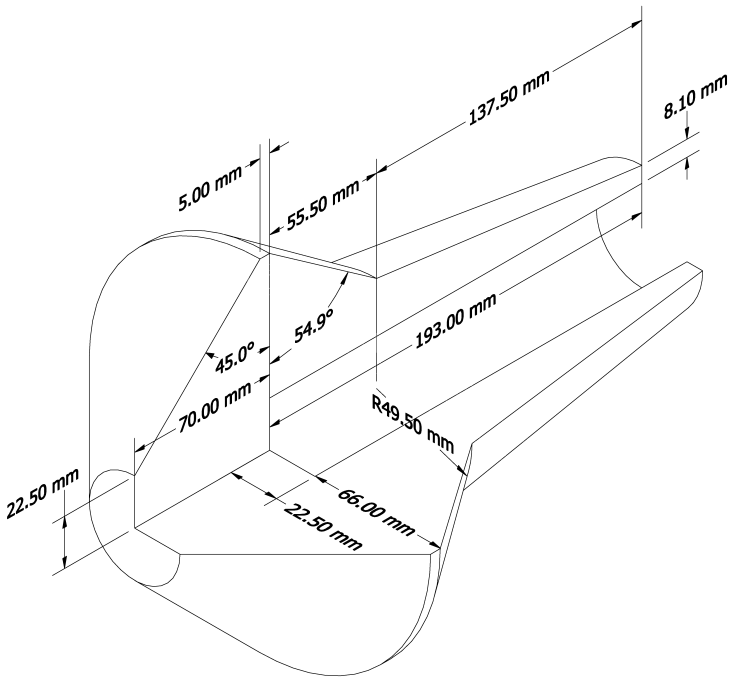

Figure 3.6: Drawing of the final geometry and dimensions of the realized polyethylene moderator

Since circular disks are placed between the source and the detector in the measurement setup (see Fig.3.10 and more general chapter 3.3.2) it is unclear to what extent d_{PE} remains the same for the final polyethylene moderator surrounding the LiI(Eu) detector at LNGS underground. Reasonably it can be assumed that d_{PE} does not depend on the neutron incident direction. However to what extent this thickness changes when the moderator is exposed to the background neutrons remains unknown.

This is since the energy spectrum of the background neutrons at LNGS underground is of course not the same as for the AmBe calibration source. But the energy range of the neutrons is about the same. It is about 2 to 10 MeV for AmBe (see Fig.5.6b) and about 0.5 to 9 MeV at LNGS underground [10], [13]. Thus it is assumed that the determined polyethylene moderator thickness of 7 cm is also valid at LNGS underground.

To verify this assumption, further measurements with the setup shown in Fig.3.10 exposed to the low neutron background at LNGS would be necessary which would take several months. Hence a lot of time can be saved by the assumption that the thermalization length d_{PE} is about the same for neutron energies in the same low MeV range.

3.2.3 Data Aquisition System

This system contains of three connected modules (see Fig.3.1), the high voltage and amplification module AMP1000-HV-E3-X4, the multi-channel analyzer Ortec Easy-MCA-8K and the Lenovo ThinkPad Edge 15 laptop.

High Voltage and Amplification Module

It generates the high voltage to operate the PMT. It also houses an amplifier to shape and amplify the voltage pulses from the PMT. The power supplied by the module is +12V DC which is transformed to the high voltage of the order of several hundred volts. The transformation factor can be adjusted by a set-screw. The value of the high voltage can be checked by a separate voltage output [19].

The generally small pulses produced by the PMT have to be amplified and shaped such that they can be fed to the MCA. This purpose serves the amplifying and shaping part of the AMP1000. First the voltage of the incoming pulse is integrated and amplified by a constant factor to produce an exponential decaying pulse with a short rise time whose amplitude, i.e. output voltage, is proportional to the area of the incoming pulse. This signal is then shaped into a bipolar semi-gaussian form, generally providing a high signal to noise ratio, and is linearly amplified to an output voltage range of 0 to 10 V [19].

Multi-Channel Analyzer (MCA)

The MCA module sorts the incoming preprocessed pulses by pulse height and stores the numbers in a histogram which contains 8192 channels (MCA channels). The sorting works by digitizing the amplitudes of the incoming pulses with an ADC and incrementing the content of an MCA channel whose address is proportional to the digitized value [10], [20].

The ADC accepts a bipolar semi-gaussian pulse with a voltage range from 0 to 10 V and a time width ranging from 0.25 to 30 μs. It compares the amplitudes, i.e. the maximum of the voltage signal, to a series of 8192 uniformly distributed reference voltages to determine the height of the pulse. The reference voltage which lies the closest to the pulse height is considered to be the digitized pulse height [10], [20].

This procedure implies a pulse height (voltage) resolution of $10/8192\ V = 0.0012\ V$ which drops if the maximal incoming pulse height is smaller than 10 V since less MCA channels would be accessible for the digitization. To maximize the MCA resolution it is therefore crucial to amplify the pulses to the required voltage window. The digitization needs sufficient time such that a minimal time between two pulses is required in order to have no signal losses, referred to as dead time, which is 2 μs [10], [20].

Laptop

The MCA memory is transferred by an USB connection to the computer software Ortec Maestro-32 installed on the Lenovo ThinkPadEdge 15 laptop. The software displays the measured histogram spectrum and saves it on the laptop in ASCII format for later processing and analysis. This data are accessible via ethernet connection.

Maestro-32 offers basically a lot of presetting, display and handling options of which the measurement time preset, job control and MCA channel threshold adjustment are used [21].

The time preset offers the possibility to measure the live time which takes account of the amount of time during which the MCA is not available to accept another pulse (i.e. is busy). It is equal to the real time minus the dead time of 2 μs (per event) where the real time is just the measurement time. I.e. by using live time the over-all statistics of two measured spectra is not affected by the dead time of the MCA.

The job control is used for the automatization of the data taking process in chapter 4.

The MCA threshold adjustment becomes useful for measurements in which a low count rate (event rate) is expected, e.g. the measurement of neutron background. The cut off of the noise peak by setting a lower channel acceptance threshold for the MCA reduces the over-all dead time of a spectrum and therefore the effective signal measurement time and simplifies the illustration of the spectrum.

3.3 Calibration

To prepare the the final measurement setup for its operation at XENON100 a calibration consisting of two stages, the γ- and neutron calibration, is necessary. First of all the LiI(Eu) detectors' capability of detecting γ-radiation is utilized in order to set the appropriate PMT operation voltage and the resulting electron gain, using ^{22}Na, ^{57}Co and ^{137}Cs sources. Then a ^{241}Am^{9}Be calibration source emitting neutron radiation is used to to calibrate the neutron signal and to determine the optimal moderation thickness of the polyethylene moderator needed in chapter 3.2.2.

3.3.1 γ Calibration and Gain Optimization

As seen in chapter 3.2.3 it is important that the signal amplitude (voltage) from the detector covers ideally all MCA channels or at least as much as possible. Since the amplification factor of the high voltage and amplification module is fixed, a signal amplification is achieved by the variation of the PMT gain. It allows the variation of the charge pulse size and therefore the variation of the signal amplitude before its amplification.

The PMT operation voltage determining the PMT gain can be adjusted by the screw which provides the high voltage and amplification module (see chapter 3.2.3). E.g. if the resulting spectra of two measurements of the same γ-calibration source differing only in the PMT operation voltage are compared with each other, the spectrum corresponding to the lower operation voltage is distributed over fewer MCA channels (see e.g. Fig.3.8a). However this voltage has to be kept within stringent limits to ensure the proper operation and the linearity of the PMT (see chapter 3.2.1).

In order to see how the variation of the PMT operation voltage affects the amplification, calibration measurements were done with three γ-ray sources, ^{22}Na, ^{57}Co and ^{137}Cs shown in Fig.3.8a and b which gives a more detailed view of the low MCA channel region. The setup for these measurements is illustrated in Fig.3.7. Each of the three γ-sources has its characteristic energy peaks. The main peak of ^{22}Na is from positron annihilation at 511 keV, the one of ^{57}Co is at 122 keV and the one of ^{137}Cs at 662 keV.

The measurement time of every spectrum was 900 s real time. Live time might have been better for the measurements but since the γ-source peaks have large statistics and the spectra are compared to each other the dead time is not crucial. Fig.3.8a and b illustrate also the stringent lower resp. upper limit on the PMT operation voltage of 600 V resp. 1000 V between which no nonlinear deformation of the spectra occur.

The PMT operation voltage shall be adjusted such that a measured neutron spectrum contains the full neutron peak. To estimate the position of a neutron peak in a γ-source calibrated spectrum is a bit difficult since the γ-radiation does not ionizes resp. excites the LiI(Eu) crystal in the same way as the α and ^{3}H-particles do. I.e. a deposition energy of 4.78 MeV (the Q-value resulting from the neutron capture in eq.(3.1)) is not situated at the expected MCA channel in a γ-source calibrated spectrum.

While heavy particles in the MeV energy range loose their energy mainly through elastic or inelastic collisions with atomic electrons, γ-particles get absorbed by the photoelectric

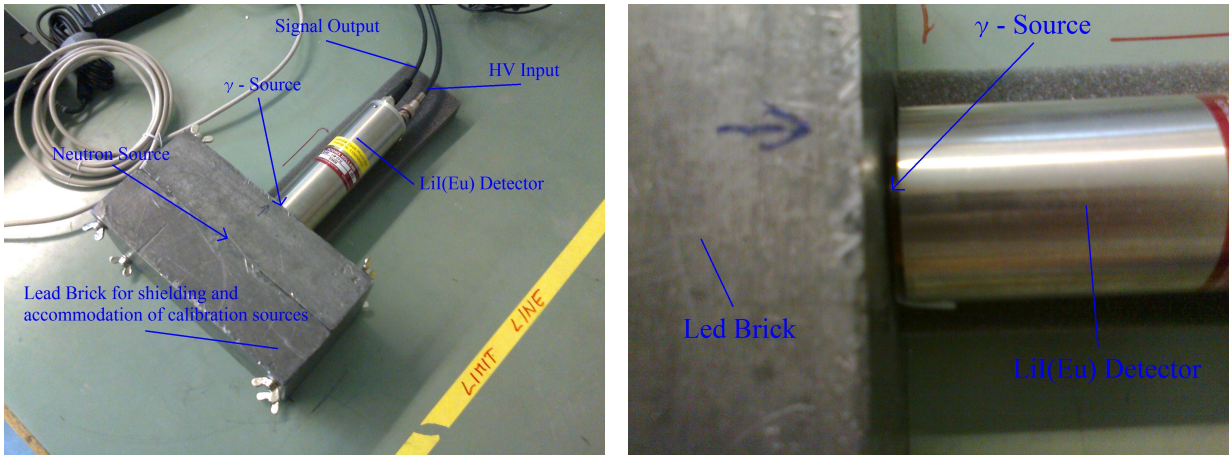

Figure 3.7: Illustration of the γ- and neutron calibration measurement setup in the UZH lab showing the overview of the setup alignment (a) and an enhanced view illustrating the γ-source placement (b). The AmBe neutron source resides within the lead block to provide a shielding of the emitted γ-radiation.

effect or pair production and scattered by the Compton effect (see appendix, chapter 5.2). In the first two processes their energy is not attenuated, i.e. there is a probability that a γ-particle has the same initial energy after flying through a certain distance in matter. Due to those three effects γ-radiation is also more penetrating compared to heavy particles. Moreover the quenching is different.

Therefore an assumption like in the case of the α and ^{3}H-particles (that they deposit all their kinetic energy inside the crystal) does not make sense for γ-particles. Such a criteria is not needed. It is sufficient if a good portion of all the γ's originating the calibration source ionize resp. excite atomic electrons of the crystal because if they interact they get absorbed in sufficient many cases (i.e. transfer their energy onto the atomic electron). If they get Compton scattered only a part of their energy is transferred to the atomic electrons resulting in a Compton continuum with a sharp upper Compton edge given by the limit case of backscattering (see Fig.3.8a).

This means in the ideal case of comparable α resp. ^{3}H and γ deposition energies in the spectrum that the size of the charge pulse resp. the signal voltage is adjusted by γ-calibration measurements such that the maximal accepted voltage of 10 V of the MCA corresponding to its highest MCA channel corresponds to a deposition energy of 5 MeV since the deposition energy is 4.78 MeV. By comparing primarily ^{137}Cs 662 keV γ-peaks for different PMT operation voltages the highest MCA channel shall correspond to a γ-deposition energy of $\approx$ 10 MeV in the real case. This high limit is picked due to the incomparability of the α resp. ^{3}H deposition energy with the γ deposition energy in the spectrum (see two text segments before) and since it has to be ensured that the neutron peak (corresponding to 4.78 MeV α and ^{3}H deposition energy) is situated inside the spectrum. In other words the 661 keV peak of ^{137}Cs shall be around MCA channel 500.

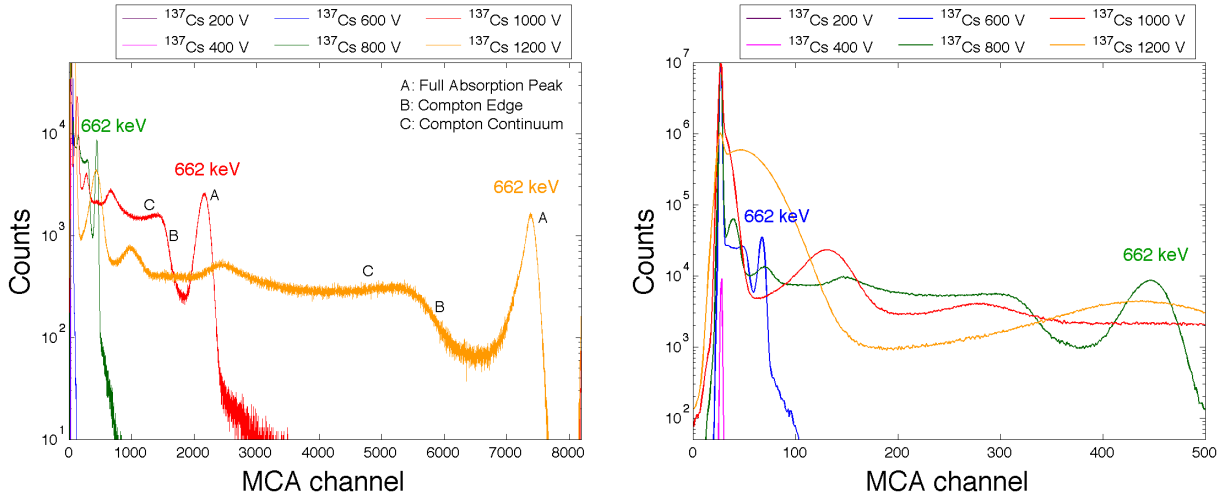

Figure 3.8: Measured γ-calibration spectra of the ^{137}Cs source for a PMT operation voltage range from 200 V up to 1200 V and a measurement time of 900 s. a) shows the full MCA channel range, b) reveals the behaviour of the spectra in the low channel range. For not too low or high voltages (within 600 V to 1000 V) the spectra show a γ-source typical behaviour. Beyond this voltage range the spectra are deformed due to nonlinear PMT gain effects.

A calibration measurement of a ^{241}Am^{9}Be neutron source provides evidence that the neutron spectrum taken with a PMT operation voltage set by this method indeed contains the neutron peak (see Fig.3.9).

The ^{137}Cs source was first used since it provides a high peak energy together with a high production rate of the 662 keV γ's. Analogous procedures for ^{22}Na and ^{57}Co confirm the found PMT operation voltage of 800 V. However, the selection of 900 V or 700 V would be also reasonable but 800 V is favoured since the detector manufacturer Scionix has tested its functionality with an operation voltage of 790 V [22].

The setup for the AmBe measurement is slightly modified compared to the one for the γ-calibration measurements: The neutron source replaces the γ-source and is placed inside the center of a $10 \cdot 10 \cdot 20$ cm thick lead brick. The purpose of the lead is to reduce the γ-background from the ^{241}Am, i.e. prevent as much γ's as possible from reaching the detector since they are the main background in such measurements. Neutrons are basically not affected by the lead.

The measurement time is changed to 11 h real time because of the low neutron activity of the AmBe source (see chapter 2.1). As illustrated in Fig.3.9 the spectrum contains the detector typical background contribution from γ's superimposed by the neutron peak. Moreover the distribution of the γ-background and neutron peak allows the separation of the neutrons from the γ's.

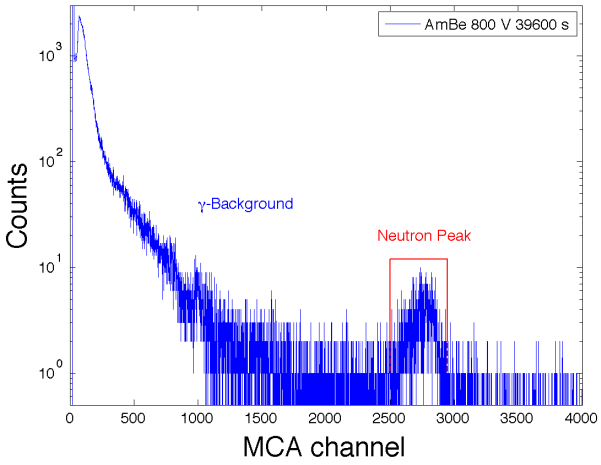

Figure 3.9: Neutron calibration spectrum from the AmBe source for a PMT operation voltage of 800 V and a measurement time of 11 h. It confirms that the γ-calibration leads to the presence of the neutron peak within the MCA channel range. The spectrum shows the typical composition of a neutron peak superimposing the considerable γ-background due to the LiI(Eu) detector sensitivity to both radiation types. Due to the distribution of the γ-background and neutron peak the neutrons can be separated from the γ's.

3.3.2 Neutron Calibration

Determination of the Moderator Thickness

In chapter 3.2.2 a polyethylene thickness of 7 cm is used for the design of the moderator. This number is found by the optimization of maximizing the neutron detection efficiency while minimizing the neutron self absorption of the moderator using calibration measurements with the AmBe source. The setup for these measurements is illustrated in Fig.3.10a.

The AmBe source is again at the center of the lead brick. The two large blocks made of paraffin ($(CH_2)_n$) shall protect people from the neutron radiation. The LiI(Eu) detector's front surface is placed at a distance of 12 cm from the leak brick which fixes the solid angle. It is then successively filled with cylindrical polyethylene disks of 1 cm thickness illustrated in Fig.3.10b such that finally twelve of them are placed between detector and the leak brick. The detector is fixed such that its symmetry axis is aligned with the one of the disks and points to the AmBe source.

Eleven measurements of 24 h live time (such that the measurements are not influenced by the dead time of the MCA (see chapter 3.2.3)) are performed. The 1 cm polyethylene disk measurement is omitted because the best efficiency is expected to be far away from 1 cm. The resulting spectra are shown in Fig.3.11 where b and d show a magnification of the neutron peak region. In order to get rid of the large γ-noise peak a lower threshold at MCA channel 200 is chosen.

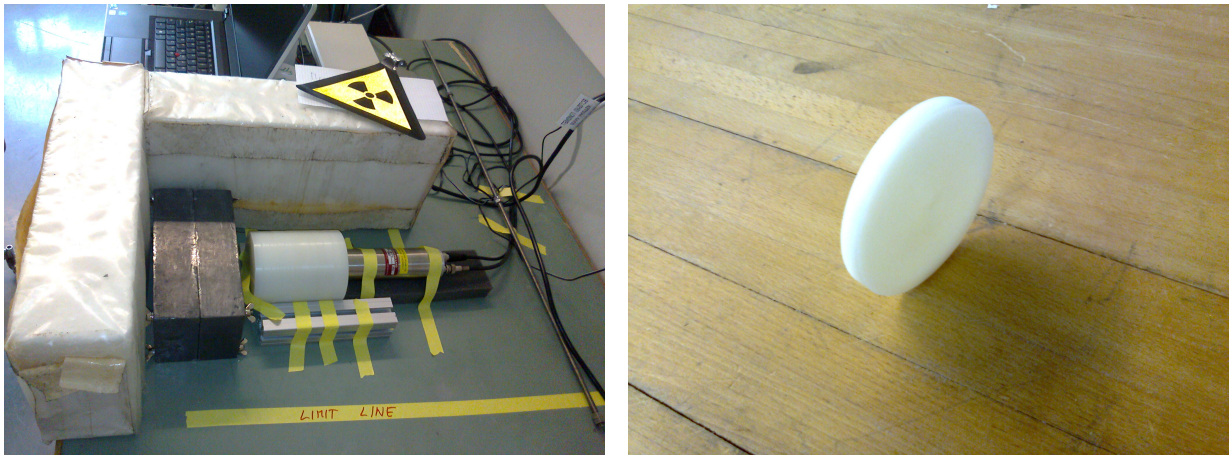

Figure 3.10: Illustration of the neutron calibration measurement setup in the UZH to find the optimal polyethylene thickness for a maximal moderation efficiency of neutrons. a) shows the overview of the setup. The disks are always close to the detector. b) shows one of the twelve polyethylene disks of 1 cm thickness. As in Fig.3.7 the AmBe source is placed within the lead block to suppress emitted γ-radiation.

At first glance the neutron peak seems to be the largest for polyethylene thicknesses ranging from 6 cm to 8 cm. In order to enable a quantitative analysis, the neutron peaks are integrated. This is just the summation of bin contents of the histograms between two boundaries. These have to be set such that they ideally enclose the entire neutron peak without any background contribution. However this is not possible since the background mainly consists of γ-radiation which is also distributed over the neutron peak. But it can be considered to be approximately the same for each measured spectrum due to the controlled PMT operation voltage (within 0.002 V uncertainty), temperature (within 5 K uncertainty) and lab environment. That means it becomes irrelevant since eleven integrated neutron peak values with the same integration boundaries are compared with each other to find the maximal value.

Therefore only the boundaries indicated by two vertical blue lines in Fig.3.11 have to be chosen appropriately to enclose the neutron peak as tight as possible (minimizing in general the background). The upper boundary is set to MCA channel 3200 because the falling shape of the neutron peak forms a sharp bend in the spectra. The lower boundary is set to MCA channel 2700. Here the desire for cutting the background results unfortunately also in rejecting a part of the neutron peak.

The integration values of the neutron peaks for the different polyethylene thicknesses are shown in Fig.3.12a. The largest amount of neutrons is observed with 7 cm polyethylene. However, the rather broad peak causes the maximal efficiency for this setup not to be reduced by more than 5% for a variation of 1 cm polyethylene.

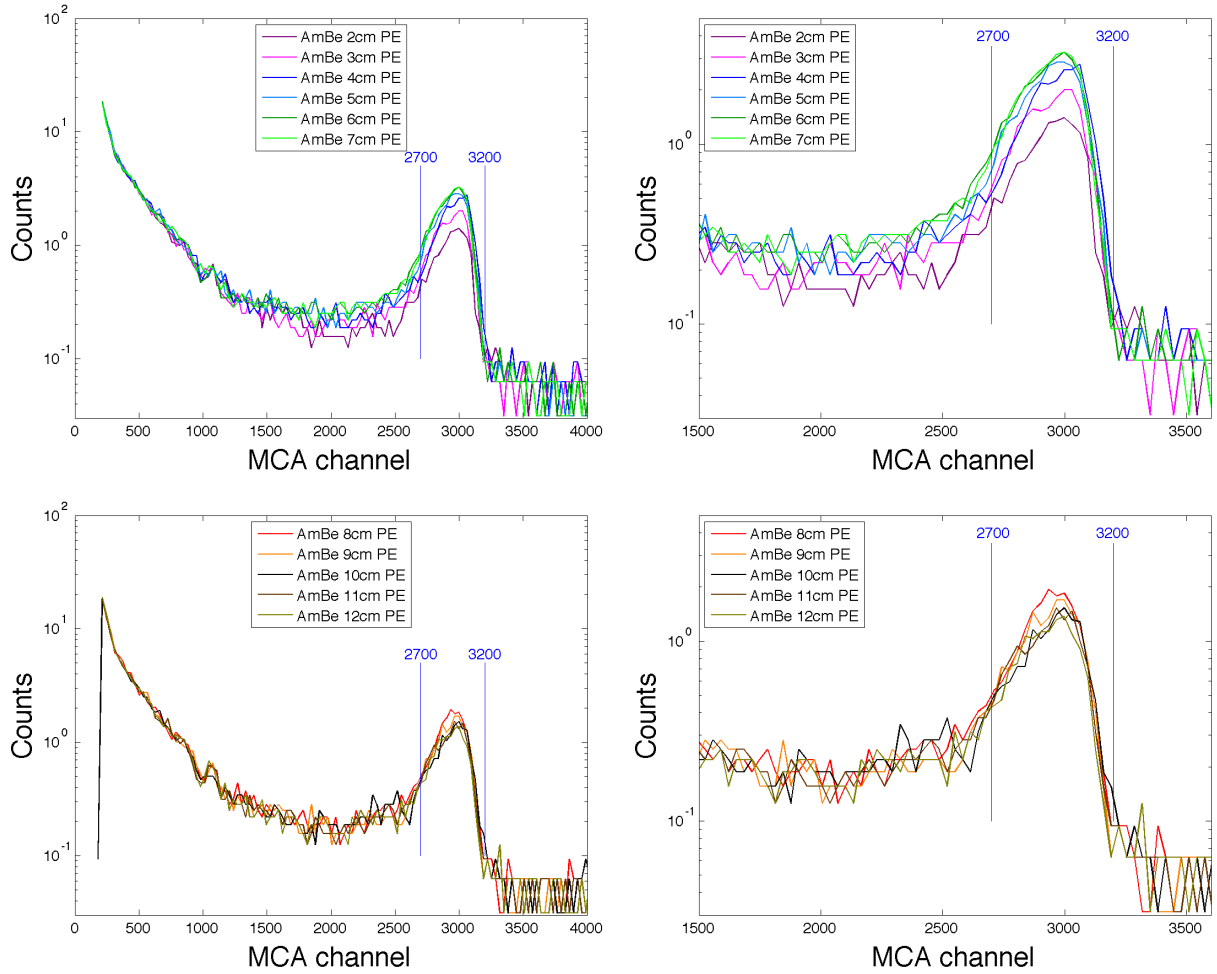

Figure 3.11: Measured neutron calibration spectra of the AmBe source to find the optimal polyethylene thickness for a maximal moderation efficiency of neutrons for a PMT operation voltage of 800 V and a measurement time of 24 h (live time). b) and d) show an enlarged view of the neutron peak. The maximal number of counts at the peak position is observed to be within 6 cm to 8 cm polyethylene. The vertical lines indicate the peak integration boundaries. The γ-noise peak at low MCA channels is omitted by a lower MCA threshold of channel 200.

In the final setup at LNGS (see chapter 3.2) the aim is to take neutron background measurements at the location of XENON100 which offers the same stable environment conditions mentioned before (actually better for the temperature). Therefore stability and reproducibility tests are performed in the UZH lab using the setup illustrated in Fig.3.10 and the same integration method as before.

These measurements verify that the neutron peak within the integration boundaries together with its underlying background remains the same for polyethylene thicknesses ranging from 4 cm to 9 cm over a period of two moths. Fig.3.12a illustrates the results given by several integration values for the corresponding polyethylene thickness. Fig.3.12b

shows the fluctuation of integration values of all measurements with 4 cm polyethylene thickness. It remains within $3 \cdot \sigma_{\text{stat}}$ [3]. The fluctuations for all other measured polyethylene thicknesses agree with the one of 4 cm.

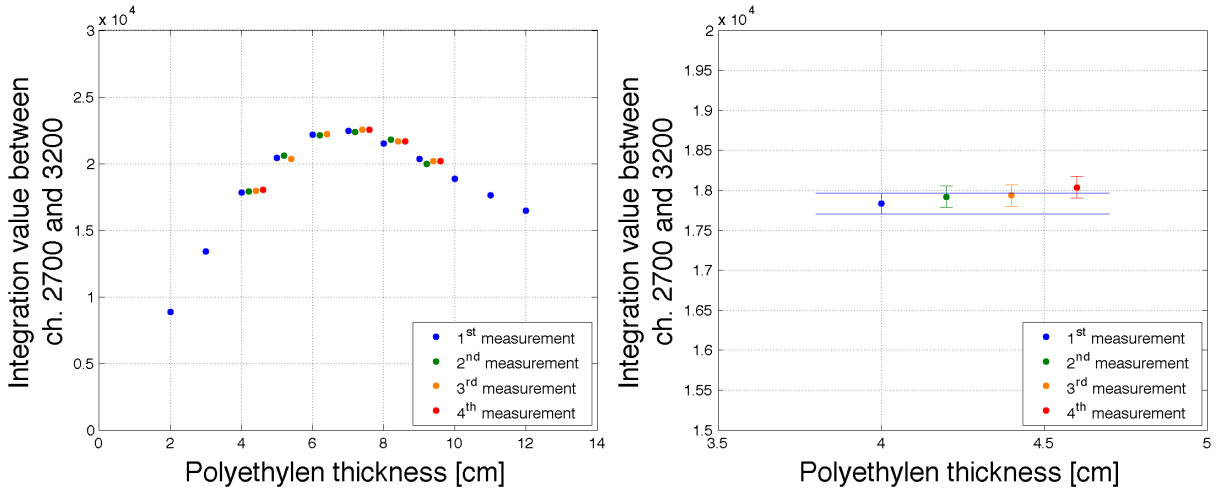

Figure 3.12: a) The result of the integration (summation of bin contents) of the neutron spectra between the indicated boundaries in Fig.3.11. The obtained values for each measurement enable the comparison between measurements of different number of polyethylene disks. 7 cm is observed to be the desired polyethylene thickness for maximal neutron capture efficiency and minimal self absorption. In addition more measurements between 4 cm and 9 cm polyethylene enable an overview of the stability of such measurements.
b) The 4 cm polyethylene measurements show that the fluctuation of the integration value is within the statistical uncertainty of the measurement. This result is confirmed with 3 times the statistical uncertainty for all other measurements in a.

Calibration at LNGS

After the stability measurements and the completion of the moderator fabrication, the final measurement setup (see Fig.3.1a and b) for the neutron background measurements at LNGS is constructed. Due to the changes made in this setup compared to the one before (confer Fig3.1 and Fig.3.10a) and the change in the environment, the γ- and neutron calibration measurements were repeated at LNGS.

Neutron calibration measurements are only rarely allowed underground as emitted neutrons might disturb other measurements, especially the dark matter searches. Thus, neutron calibration measurements were done in the XENON lab on the surface at LNGS. Fig.3.13b shows the arrangement of the box and the sources for the measurements. The measurements were done using a ^{137}Cs source of 74 kBq activity, a ^{57}Co source of 74 kBq,

[3] Due to the integration (summation) method, the statistical error on the integration value is:
$\sigma_{\text{stat}} = \sqrt{N}$,
where N is the sum of all bin contents between the integration boundaries.

as well as a $^{241}Am^{9}Be$ source of 3.2 MBq americium activity which yield about 220 neutrons per second. The measurement time was 11000 s $\approx$ 3 h live time for the γ-sources and 12 h live time for the AmBe source. Fig.3.14a shows the resulting spectra.

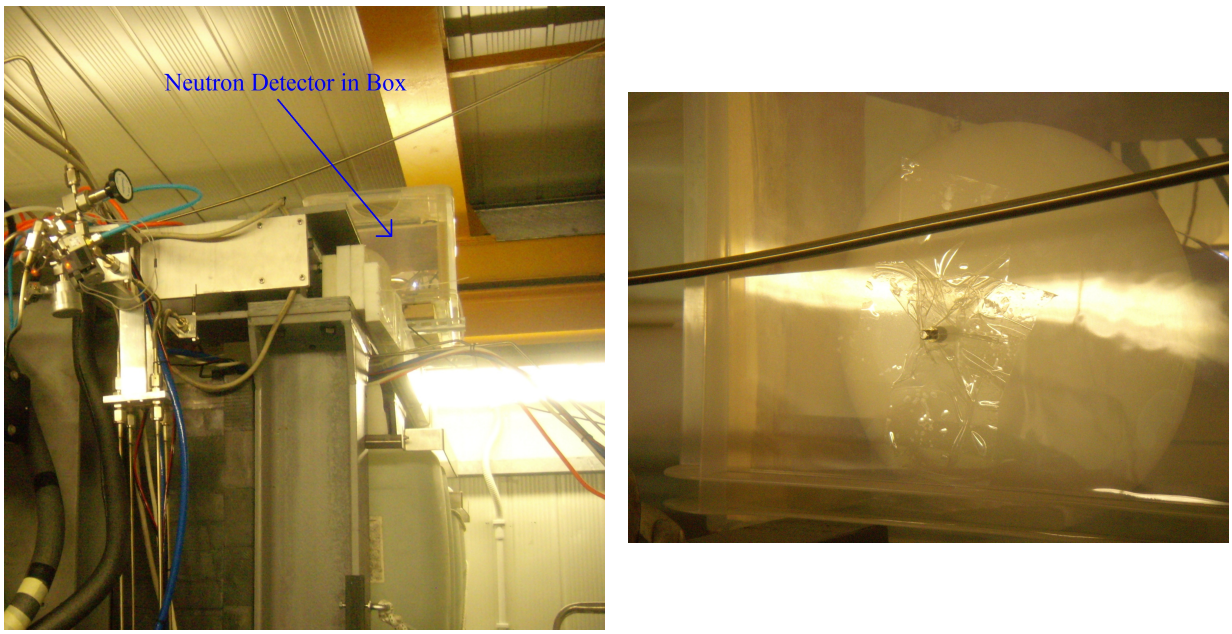

Figure 3.13: a) Location of the final measurement setup on top of XENON100 underground at LNGS for the γ-calibration- and neutron background measurements.
b) Placement of the calibration sources directly in front of the moderator at the outer side of the box. A marker on the plastics ensures that every source can be fixed at the same position.

Additionally, the two γ-source measurements were taken at the final location underground a few days later. They were done in the same way as the measurements above ground with the sources at the same relative position to the detector except for a shorter measurement time of 1 h live time, still providing enough statistics. The shorter measurement time is due to the fact that γ-source calibration measurements weren't allowed during the dark matter data taking time of XENON100, i.e. they had to be done while XENON100 was taking calibration data. Fig.3.13a and b illustrate the box and the sources on top of the XENON100 shield underground. Fig.3.14b shows the resulting spectra.

The γ-and neutron spectra are changed due to the different setup and environment. But since the ^{137}Cs 662 keV peak and the neutron peak are in the same MCA channel region as in the case of the γ-calibration in the UZH lab before the PMT operation voltage of 800 V is not changed. Therefore the integration boundaries are primarily not changed.

With the location change from the XENON lab on the surface to XENON100 underground there is again a change in the environment. This change becomes crucial since the spectrum from the AmBe calibration measurement on surface is used as a comparision.

To get an idea of how much the environment change affects the measured spectra, Fig.3.15a shows the γ-source measurements taken in the XENON lab and underground

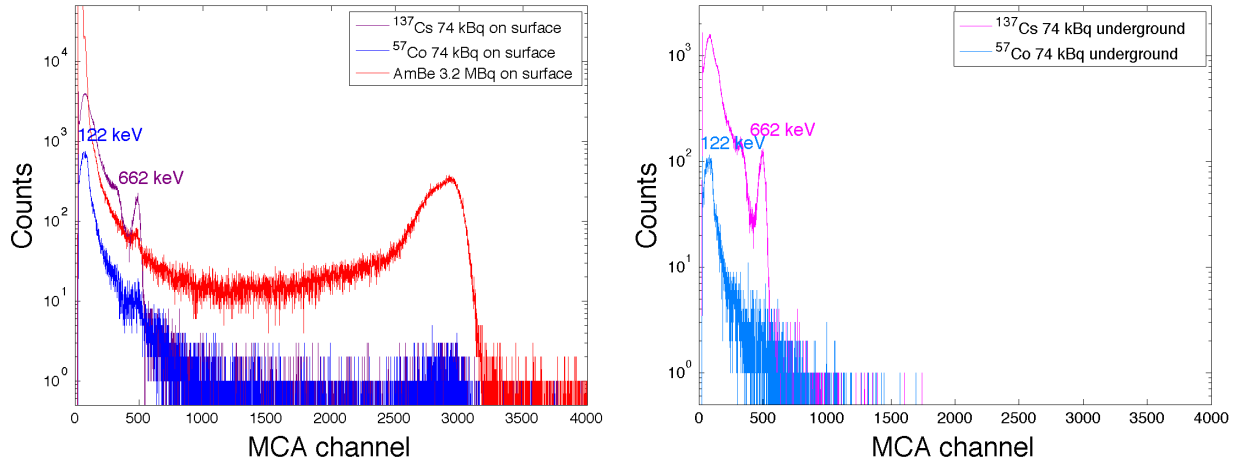

Figure 3.14: Measured calibration spectra of ^{137}Cs, ^{57}Co and AmBe neutrons on surface in the XENON lab (a), and ^{137}Cs and ^{57}Co source underground on top of XENON100 (b). The measurement time for the γ-source measurements on surface is 11000 s, for the AmBe source 12 h and for the γ-source measurements underground 1 h (all live time). The small peak around MCA channel 2900 in the γ-spectra in a might be due to neutron capture of environmental neutrons. It does not exist in the γ-spectra in b since the neutron background underground is considerably lower than on surface.

at XENON100. The 662 keV peak of ^{137}Cs underground is shifted upwards by about 10 MCA channels.

Fig.3.15b shows the AmBe source measurement from the surface and the first 6 weeks of measurement data of the neutron background underground. The small neutron peak from the underground measurement is shifted downwards about 400 MCA channels compared to the neutron peak for the surface measurements. This shift is totally different from the one observed for γ-spectra.

Due to the low neutron flux underground, it can be that the small background peak does not show the α's resp. ^{3}H's originating from the neutron capture but ones from different sources. These are mainly the scintillation crystal of the detector itself or the air directly surrounding the scintillation crystal. To verify this statement the background spectrum was compared to another background spectrum taken inside a neutron shield of 20 cm polyethylene thickness with another identical LiI(Eu) detector and a similar setup shown in Fig.3.16a, b and Fig.3.17.

Due to the slightly different operation voltage of the detector and the generally different PMT gain the two background spectra are shifted to one another by a linear function (see Fig.3.18a). In order to get rid of this shift the peak position of peak 2 is shifted downwards to the position of peak 1. The peak position is considered to be where the peak's maximum is located. The resulting spectra show Fig.3.18b in which the counts are replaced by the rate in order to make the spectra measurement time independent.

The two background peaks are observed at similar MCA channels. To quantify their

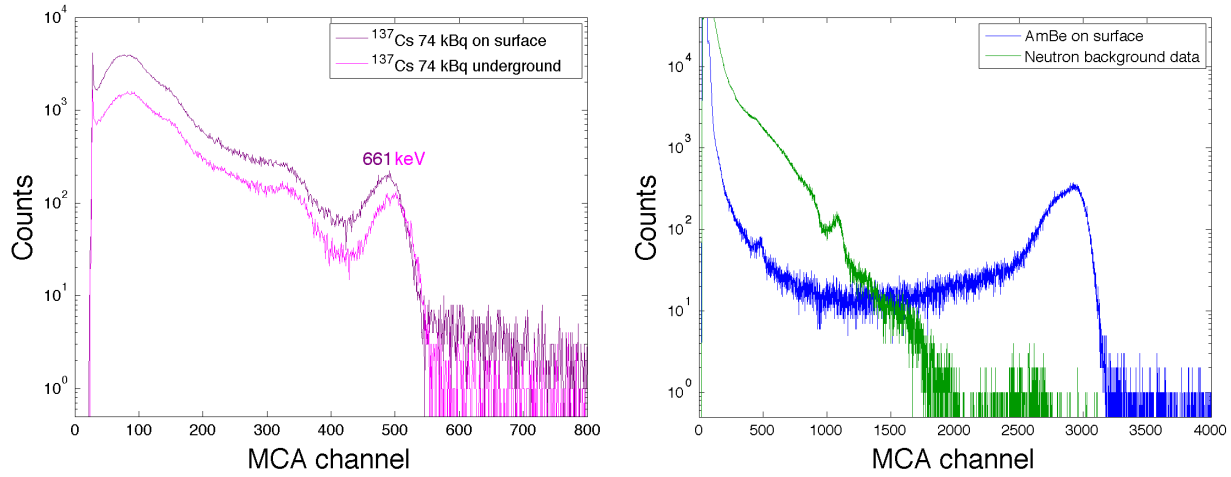

Figure 3.15: a) The measured ^{137}Cs γ-spectra on surface and underground from Fig.3.14 a and b displayed together to allow for a comparison revealing the small MCA channel shift of about 10 channels.
b) The measured AmBe spectrum on surface from Fig.3.14 a and the neutron background spectrum containing the first six weeks of data. The small peak in the background spectrum at about MCA channel 2900 is shifted down roughly by 400 MCA channels.

agreement the two peaks are integrated as before in the case of the AmBe calibration measurements by using the same criteria to find the integration boundaries. These were set at MCA channel 2120 and 3200.

The resulting integration values are integrated rates due to the normalization by introducing rates. Within the statistical error the values agree (see Tab.3.1). Therefore the small peak of the background spectrum taken at XENON100 really shows mainly background α's and not events from neutron capture. This is since the neutron flux is highly suppressed due to the polyethylene shield and mainly the α-background contributes to the events at high energy.

Although no AmBe calibration measurement taken underground for the direct comparision with the measurement on surface is available the change of the neutron peak position can be assumed to be small due to the small change in the case of γ-calibration measurements. Hence the upper integration boundary of MCA channel 3200 is used for the integration of the neutron peak in the neutron background spectra underground as well.

The large α-background requires to set a new lower integration boundary for the neutron background measurements to minimize the contribution from the α's. For this the spectra of the AmBe source measurement on the surface and the neutron background measurements underground are considered again, but now normalized to the same peak height shown in Fig.3.19. A spectrum integration from MCA channel 2000 to 3200 for AmBe on surface and MCA channel 2120 to 3112 for neutron background yield two cumulative distributions shown in Fig.3.20a. The distribution for the neutron background is inverted such that the

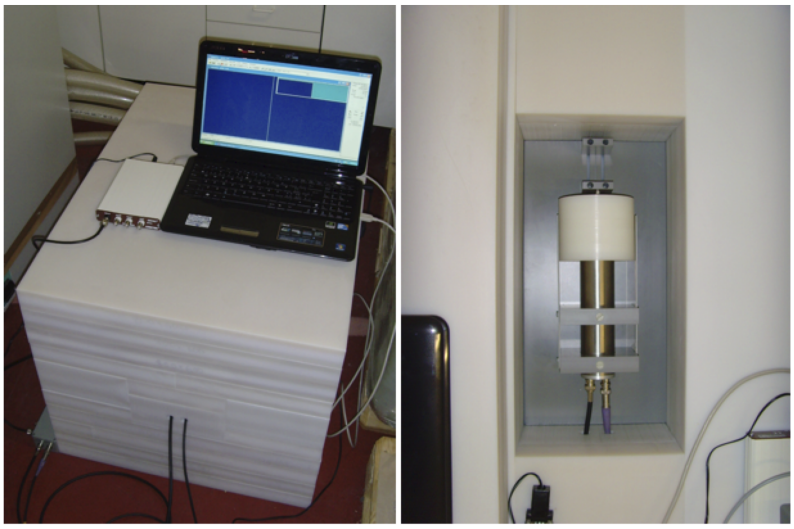

Figure 3.16: a) The similar detection system for the measurements inside the neutron shield. The LiI(Eu) detector is fully mounted in a shield box consisting of borated polyethylene with 20 cm wall thickness.
b) The view inside the neutron shield after the top shield layers have been removed [23].

overlap of these two curves gives an idea of how large the contamination of background α's is for the AmBe source measurement.

Of course the α-background contamination should be minimal (high α-rejection) with a maximal neutron acceptance. Following this principle a star marker is placed on a salient point of the neutron background curve in Fig.3.20a. This point yields a lower neutron acceptance than choosing the intersection point of the two curves, however, the contamination is lower which is preferable in this case. The vertical blue line through the star marker yields the lower integration boundary at MCA channel 2729. The horizontal line through the dot marker indicates a neutron acceptance of 80.25%. Thus the final neutron detection efficiency has to be lowered by this acceptance.

Fig.3.20b illustrates the final integration boundaries for the neutron background measurements with the AmBe calibration measurement on surface and the neutron background measurement underground.

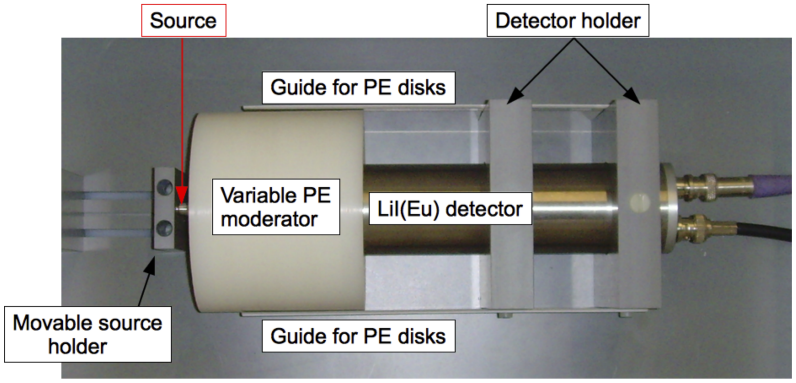

Figure 3.17: The superstructure of the LiI(Eu) detector setup. The detector tube is fixed by two holders. The moderator block consists of 1 cm thick polyethylene disks which are centered by two lateral side-guides. The source can be mounted on a source holder which is movable along the symmetry axis of the detector [23].

	Integrated Rate $[s^{-1}]$
Background underground	$(8.9 \pm 0.5) \cdot 10^{-5}$
Background inside neutron shield	$(9.13 \pm 0.3) \cdot 10^{-5}$

Table 3.1: The integration of the two neutron spectra in Fig.3.18b yield values which are fully consistent within their statistical error. Hence the contribution to the peak is indeed not from neutrons but from background α-particles. They are emitted from radioactive contamination inside the detector crystal or the air (e.g. Radon) closely surrounding the crystal.

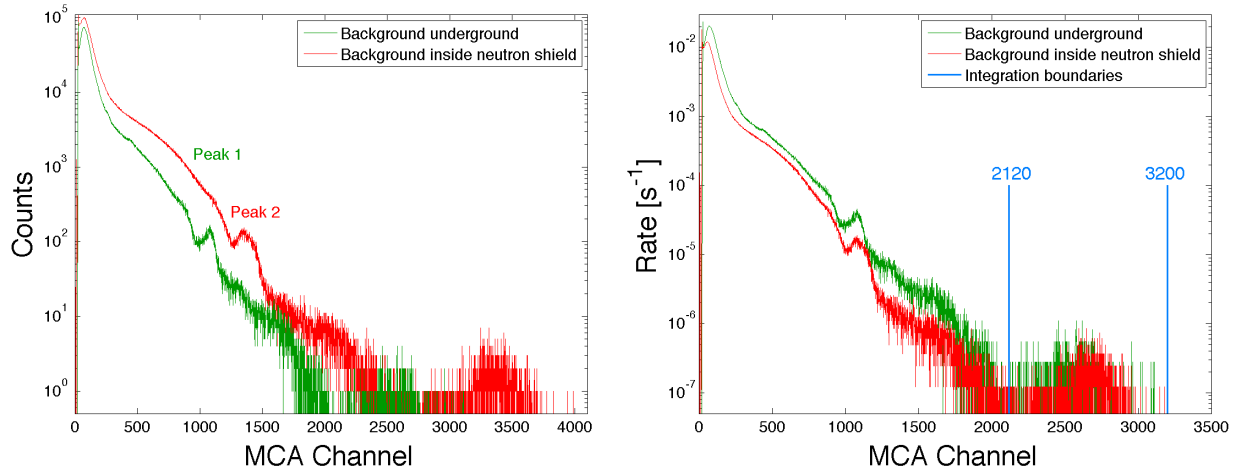

Figure 3.18: Examination of the reason for the of the neutron background peak "shift" in Fig.3.15b:
a) The neutron background spectrum measured with the final measurement setup and a neutron background spectrum behind a neutron shield measured by an analogous setup using an identical LiI(Eu) detector [23]. Different PMT gains, backgrounds and measurement times cause the shift in MCA channels and counts.
b) The same two spectra as in a converted to the same MCA channel axis and scaled by measurement time. The two peaks are observed to be very similar. Therefore, they might have the same origin which could not be from neutrons since they are highly suppressed in the neutron shield.

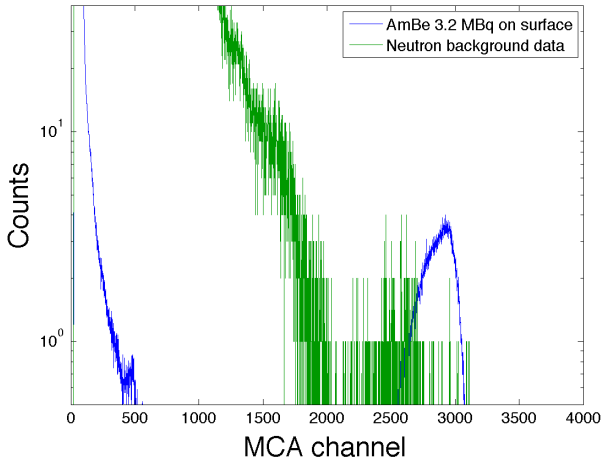

Figure 3.19: The spectra of the AmBe source on surface and the neutron background illustrated in Fig.3.15b normalized to the same peak height. They do not agree with each other but have an overlap.

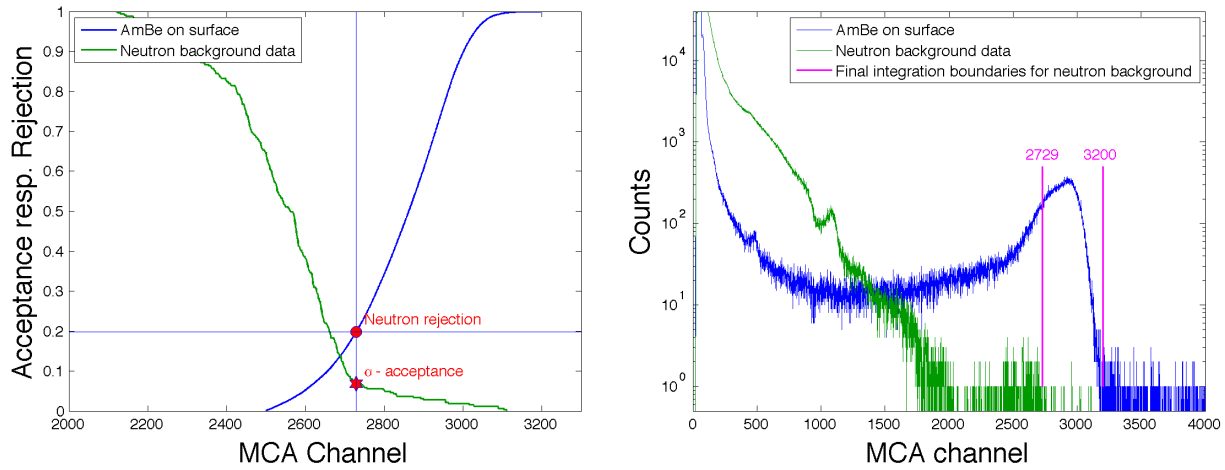

Figure 3.20: a) To determine the lower integration boundary for the highest possible α-rejection and highest neutron acceptance, the bin content within the peak boundaries is integrated up to the respective MCA channels (see Fig.3.19). The curve from the neutron background spectrum is inverted and crosses the one from the AmBe calibration spectrum. The star marker at MCA channel 2729 indicates the position satisfying minimal neutron- and maximal α rejection. The horizontal blue line crossing the dot marker points to the percentage of rejected neutrons. The efficiency is reduced by about 20%.
b) Similar to Fig.3.15b but with the final lower integration boundary determined by the rejection optimization shown in a. The upper boundary remains unchanged.

4 Neutron Flux at LNGS

The calibration of the detector together with its final measurement setup enables the monitoring of the neutron count rate. This data was acquired automatically and provided in an easily accessible form. Therefore a data processing chain is required. Here, the methods used to obtain the neutron count rate data are presented followed by the results itself.

The discussion covers the interpretation of the results. The measured resp. simulated neutron flux [13] determines the expectation at which neutron count level a fluctuation can be observed. This is then compared with observed neutron counts from our neutron background measurements to reveal if a fluctuation is observable for different time intervals and how it behaves. In addition the neutron flux is calculated from the neutron monitoring results and compared with the neutron flux independently measured at XENON100. This enables the estimation of an overall efficiency of the detection system. Finally the outlook gives an overview of development possibilities to improve the detection system.

4.1 Data Acquisition and Analysis for Neutron Monitoring

After the installation of the box at its final position on top of the XENON100 shield at LNGS (see Fig.3.13a) and the γ-calibration measurements, the setup (see chapter 3.2) takes neutron background data since July 1, 2011. It provides an ASCII .Spe file which contains the spectrum, the starting time of the data acquisition and its predefined duration along with other information such as dead time.

To determine the neutron rate, the spectrum is integrated between the integration boundaries set by the neutron calibration (see chapter 3.3.2) which yields one value per measurement. Since the time evolution of the neuron count rate is of interest here, many values are needed. A routine in the acquisition program Maestro-32 is set up to start a measurement automatically after a given time interval. The duration is chosen to be 24 hours. Several spectra can be added later to cover larger time intervals. The .Spe files are saved in a folder on the data acquisition laptop.

When the data acquisition is automatized by Maestro-32, the integration of the spectra has to be automatized as well. This is a achieved by implementing the integration algorithm in a C++ program which is able to read the ASCII .Spe spectrum. It provides the integration value, i.e. the rate for a day, along with the starting time in Unix Time Stamp format, the path of the file and the statistical error on the integration value. The program is executed in a bash script using the latest acquired .Spe file as an argument. Finally, a Cron Job, an unix environment tool, executes this Bash Script every 24 hours after a new measurement is delivered by Maestro-32.

The analysis, i.e. the execution of the bash script, is done on the Linux cluster of the XENON collaboration at LNGS. The .Spe files are transferred from the laptop to the xecluster using rsync, another Unix environment tool, which is started by the Bash Script as well. All measured daily neutron rates together with the information needed for the visualization process described in the next chapter are stored in a text file on xecluster.

In order to visualize the time evolution of the neutron rate, the rates in the text file have to be plotted versus time. The analysis program ROOT allows for the execution of C files containing the plot routine in the bash script. It creates a new rate plot (png file) including all available data. For convenience the Unix Time Stamp is converted into local time.

To provide the time evolution to the XENON collaboration, the png file is transferred automatically to a webpage on the UZH web server again using rsync. Therefore the time evolution of the neutron rate is updated automatically and daily. As an example, Fig.4.1a shows the time evolution of the neutron rate from the 1st of July to the 11th of August. In addition the latest 24 h spectrum is displayed on the webpage, shown in Fig.4.1b.

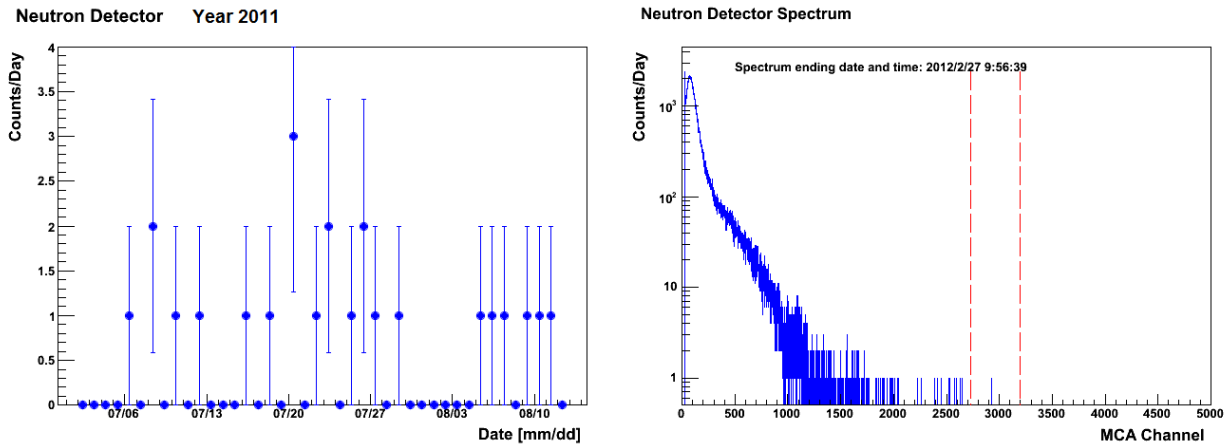

Figure 4.1: a) The time evolution of the daily neutron count rate. The data acquisition provides one spectrum per day. It is automatically integrated by a C++ program yielding one value per day, plotted versus the finishing date of the spectrum. In this case the data from July 1 to August 11 2011 (6 weeks) is shown.
b) The latest measured daily spectrum. The red dashed vertical lines indicate the integration boundaries used by the C++ program.

When the evolution of the neutron rate covers larger time periods than weeks, it becomes reasonable to display it weekly not daily since the larger binning allows for the visualization of fluctuations which are invisible on a daily basis. Its implementation in the analysis procedure consists of a little extension in the C++ program which adds 7 daily spectras and creates then a text file containing the data for a week. Every week the integration algorithm yield an additional neutron rate value which is plotted versus the time analogous to the daily neutron rate.

Another png file (see Fig.4.2a) is created and transferred to the webpage. The latest weekly spectrum is also displayed on the webpage (see Fig.4.2b). Fig.4.2c shows all collected data, in this case the 6 weeks of data. In order to get this plot the C++ program was slightly modified yielding an additional text file containing the sum of all collected spectra and an additional plotting routine for ROOT was included in the bash script.

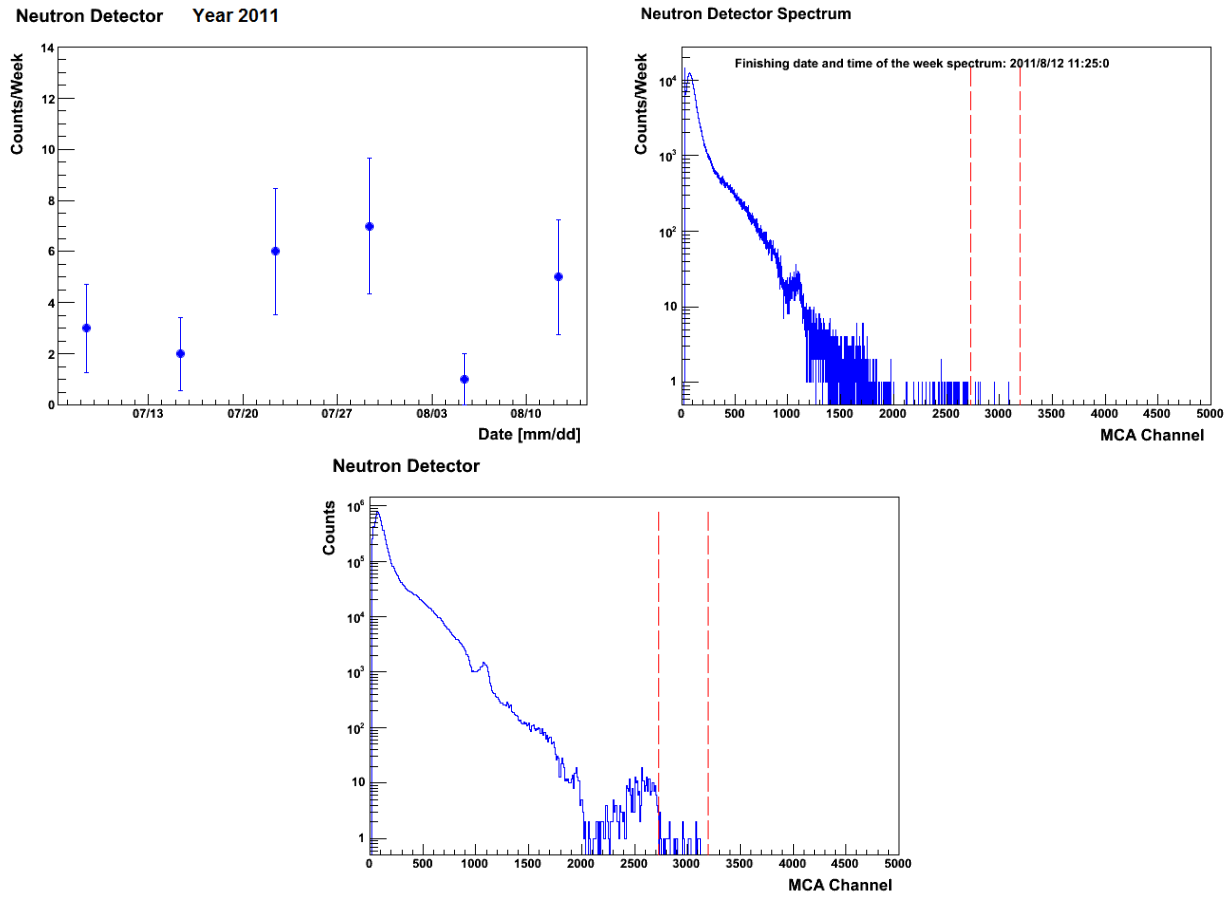

Figure 4.2: a) The time evolution of the weekly neutron count rate. Seven of the daily spectra delivered by Maestro-32 (see e.g. Fig.4.1b) are added and integrated by the C++ program automatically. This yields one value per week, plotted versus the finishing date of the last spectrum contributing to the week. The same time period for the data as for Fig.4.1a (6 weeks) is considered.
b) The latest weekly spectrum. The red dashed lines indicate the integration boundaries used by the C++ program.
c) The summation of all the spectra measured between July 1 and August 11 2011. Again, the red dashed lines indicate the integration boundaries. In this case they are not used for an integration but are placed to show the calculated boundary between neutron peak and intrinsic α-background (see chapter 3.3.2).

4.2 Results: Time Evolution of Neutron Count Rate

The latest plots corresponding to Fig.4.1 a, b and Fig.4.2 a, b, c are updated daily and can be found on the webpage:
http://www.physik.unizh.ch/groups-/groupbaudis/xenon/restricted100/ndet_lngs/neutronAnalysisRes
Fig.4.3a and b show the analysis results from July 1, 2011 until May 1, 2012. The gap in the data between August and October 2011 is due to a crash of the data acquisition system

at August 12, 2011. The problem causing this crash could not be solved until October 17, 2011. Since then the data is again taken properly.

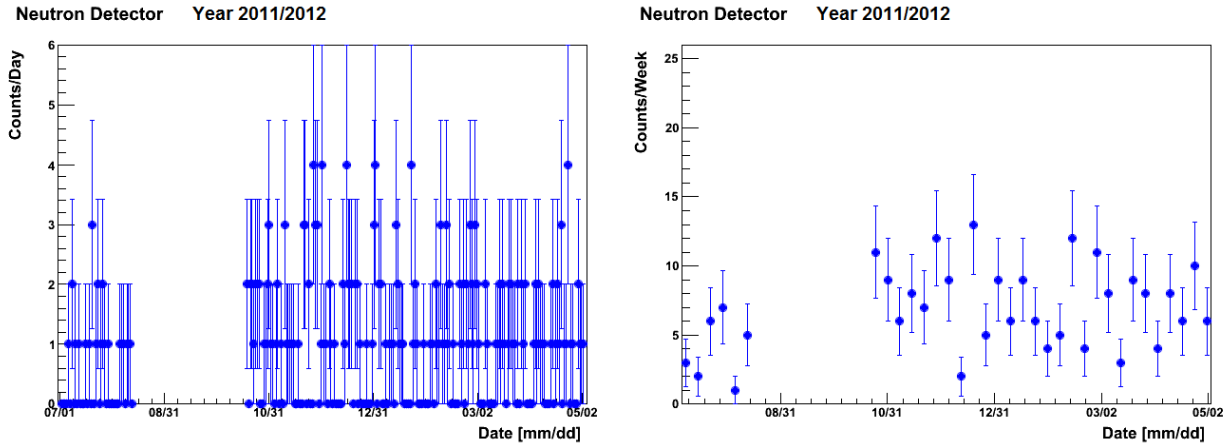

Figure 4.3: a) Analogous to Fig.4.1:
In this case the data from July 1 2011 to May 1 2012 is considered. The data has a gap from August to October 2011 since the data acquisition system crashed at August 12. The problem causing the crash could be solved and it again provides data properly since October 17. A larger binning is given in b.
b) Analogous to Fig.4.2:
The same time period for the data as for a, i.e. from July 1 2011 until May 1 2012, is considered. Again, the data has a gap from August to October 2011 since the data acquisition system crashed at August 12. The problem causing the crash could be solved and it again provides data properly since October 17.

4.3 Discussion

In order to reveal the sensitivity to fluctuations in the neutron rate, the neutron flux from [13] is converted into counts per time interval. The results give an overview of how much counts per time interval are expected.

In [13] the neutron fluxes are location dependent. According to the Monte Carlo simulations performed the total neutron flux calculated is shown in Tab.4.1. The uncertainties given are attributed to the uncertainties in the neutron production rate from (α,n) resp. fission reactions and the uncertainty in the neutron energy. The overall systematic uncertainty of the total neutron flux is estimated to be around 20%. There uncertainties are not considered in the following calculations.

The typical water content in the concrete is 12% with a possible variation of 4% at most. Since a differing water content causes differing neutron moderation, dry (H_2O content 8%) and wet concrete (H_2O content 16%) are taken into account for the Monte Carlo simulations in Hall A. The concrete thickness underground at LNGS is at least 30 cm. According to [13] neutrons with an energy $E > 1$ MeV are produced mainly in the concrete supporting the

inside hall walls. Therefore the different radioactive contaminations in the rock surrounding the concrete of hall A and hall C contribute much weaker than in the case of no concrete.

XENON100 is neither located in hall A or C but in a different part of the underground laboratory (see Fig.1.1). However we use the values of [13] for our calculations as measurements show ([24]) that the neutron flux at the XENON100 location agrees with the numbers from [13].

Monte Carlo simulations of the total neutron flux at LNGS (10^{-6}cm^{-2}s^{-1})	
Hall A, dry concrete:	3.75 ± 0.67
Hall A, wet concrete:	1.67 ± 0.29
Hall C, dry concrete:	2.26 ± 0.49

Table 4.1: The total neutron flux in hall A and C underground at LNGS (see Fig.1.1 for location). This flux is the result of Monte Carlo simulations in [13]. Different water contents in the concrete supporting the outer walls under ground were taken into account for the simulation. Dry concrete has a water content of 8%, wet concrete 16%. The uncertainties given are only attributed to the uncertainties in the neutron production rate from (α,n) and fission reactions and the uncertainty in the neutron energy. The overall systematic uncertainty of the total neutron flux is estimated to be around 20%.

Starting with a flux ϕ, the counts n per time interval t are given by

$$n = \phi \cdot S \cdot t \quad , \tag{4.1}$$

where S is the LiI(Eu) crystal surface. According to its dimensions (see chapter 3.2.1) and the surface formula of a cylinder

$$S = 2\pi r\,(h + r) \quad , \tag{4.2}$$

where r is its radius and h its height, it is $S_{\mathrm{LiI(Eu)}} = 12.528$ cm^2. For the calculation the mean value of the 3 neutron fluxes in Tab.4.1 of $\phi_{\mathrm{mean}} = 2.56 \cdot 10^{-6}$ cm^{-2}s^{-1} is taken. This value is converted into a neutron rate according to eq.4.1 for various time intervals (see Tab.4.2).

Additionally an upper and lower value are calculated for each time interval. Above the upper or below the lower value the statistical 1σ-error of the converted neutron rate and another neutron rate value do not overlap. In this case, the criteria of a visible fluctuation is assumed to be fulfilled. Thus the upper and lower value tell at which neutron rate value a fluctuation becomes observable. Their differences to the converted neutron rate value are also expressed in percent.

From Tab.4.2 it can be concluded that a neutron flux variation at the 20% level should be visible within a binning (time interval) of 5 weeks, if the detector efficiency is assumed to be 100%. In reality it is of course lower but still expected to be good since the neutron

Time Interval	Converted Rate	Upper Value		Lower Value	
1 week	19.4	29.2	50.5%	11.6	40.2%
2 weeks	38.8	52.3	34.8%	27.3	29.6%
3 weeks	58.2	74.4	27.8%	43.9	24.6%
4 weeks	77.6	96.2	24.0%	61.0	21.4%
5 weeks	97.0	117.7	21.3%	78.3	19.3%
6 weeks	116.4	139.0	19.4%	95.8	17.7%
7 weeks	135.8	160.1	17.9%	113.5	16.4%

Table 4.2: The neutron rate converted from the MC simulations of the neutron flux in Tab.4.1 for binnings (time intervals) of 1 until 7 weeks. Only the mean value of the 3 neutron fluxes is used for the conversion. An upper and lower value is calculated such that, if a another neutron rate value is above or below these values, the statistical 1σ-errors of the two rates do not overlap. In this case the criteria of a visible fluctuation is assumed to be fulfilled. The for upper and lower values are also given in percent of the difference to the corresponding neutron rate value.

peaks in the spectra are at thermal energies due to the moderator and the high capture cross-section of ^{6}Li for thermal neutrons maximizes the efficiency of this experiment.

The neutron rates in Tab.4.2 are compared with the measured ones shown in Tab.4.3. It lists the available neutron rate data of 24 weeks with a 6 week binning such that the time interval for one neutron rate value is 6 weeks. In contrast to the value in Tab.4.2 for the 6 week time interval, the measured values are smaller. Analogous to Tab.4.2 the upper and lower values of the measured neutron rates are calculated and their differences to the measured neutron rate value are expressed in percent. They are larger than in Tab.4.2 due to the smaller corresponding neutron rate value.

From Tab.4.3 can be concluded that a neutron flux variation at the 30% to 40% level becomes visible within a binning (time interval) of 6 weeks. In Tab.4.2 the variation is at a level of about 18.5% for the same binning. The values become comparable when the binning for the neutron rates in Tab.4.2 becomes smaller, i.e. if the values per 2 weeks are considered. This discrepancy is expected since the overall detector efficiency is lower than 100%.

Additional tables like Tab.4.3 exist which list the available amount of measured neutron rate data with a different binning (time interval), i.e. from 1 until 7 weeks. They are shown as plots in Fig.4.4. If a fluctuation is observable between 2 measured neutron rate values, i.e. if their statistical 1σ-errors do not overlap, a star marker is placed between them.

In Fig.4.4a several fluctuations of the measured neutron rates are observed for the 1 week time interval, basically 3 times 3 subsequent fluctuations every 6 or 7 weeks within the available data of 34 weeks. However the rate value does not increase or decrease significantly, but it remains at the same level before and after the fluctuation. This kind of fluctuation is not the one desired to reveal. The one to look for shall be visible over time intervals of months by changing the rate value level significantly. When changing

Time Interval	Measured Rate	Upper Value		Lower Value	
6 weeks	24	34.8	45%	15.2	36.7%
	53	68.6	29.4%	39.4	25.7%
	44	58.3	32.5%	31.7	28.0%
	40	53.6	34.0%	28.4	29.0%
	43	57.1	32.8%	30.9	28.1%

Table 4.3: The measured neutron rates for a binning (time interval) of 6 weeks. 34 weeks of data are present in total, but only 30 weeks are available for the binning. Analogous to Tab.4.2 the upper and lower values are calculated such that, if the subsequent measured neutron rate is above or below these values, the statistical 1σ-errors of these two do not overlap. In this case the criteria of a visible fluctuation is assumed to be fulfilled. The values for upper and lower limits are also given in percent of the difference to the corresponding neutron rate value.

the binning (change the time interval to larger amount of weeks) most of the insignificant fluctuations disappear. E.g. for the 5 week binning in Fig.4.4e only one is observable.

Therefore up to now the neutron rate is around a constant level. An in- or decrease can not be observed yet due to the lacking amount of data or due to the indeed constant neutron flux.

A further calculation gives an estimation of the overall detector efficiency. To get this quantity, the simulated neutron flux in Tab.4.1 from [13], the LiI(Eu) crystal surface of $S_{\mathrm{LiI(Eu)}} = 12.528\ \mathrm{cm}^2$, the sum of all daily neutron rates provided by the detection system and the total measurement time are inserted into eq.(4.1) and solved for the measured flux $\phi_{\mathrm{meas}} = 0.91 \cdot 10^{-6}\mathrm{cm}^{-2}\mathrm{s}^{-1}$. The ratio of the measured and the predicted neutron flux yields the estimation of the detector efficiency. It is about 36% which is adequate for such a detector.

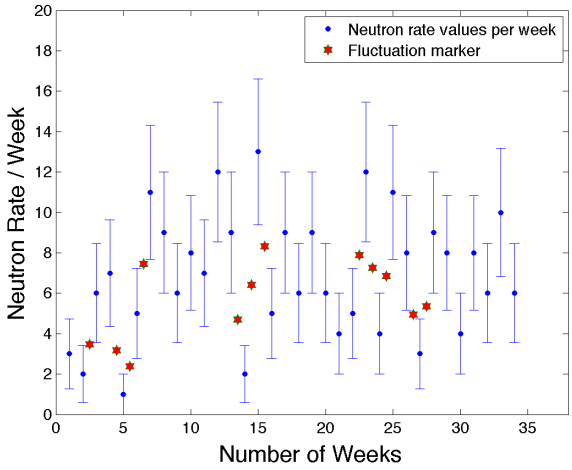
Neutron rate values per week
Fluctuation marker
Neutron Rate / Week
Number of Weeks

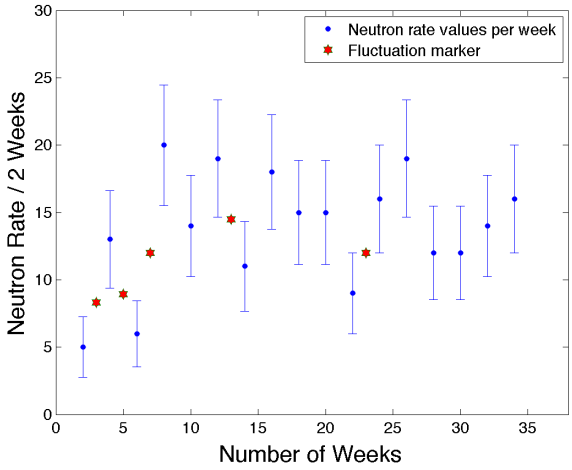
Neutron rate values per week
Fluctuation marker
Neutron Rate / 2 Weeks
Number of Weeks

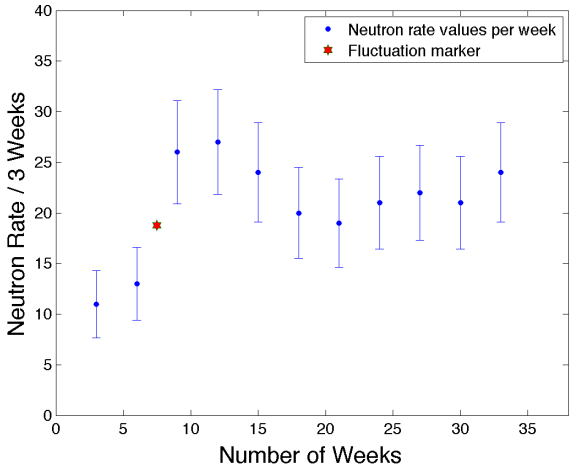
Neutron rate values per week
Fluctuation marker
Neutron Rate / 3 Weeks
Number of Weeks

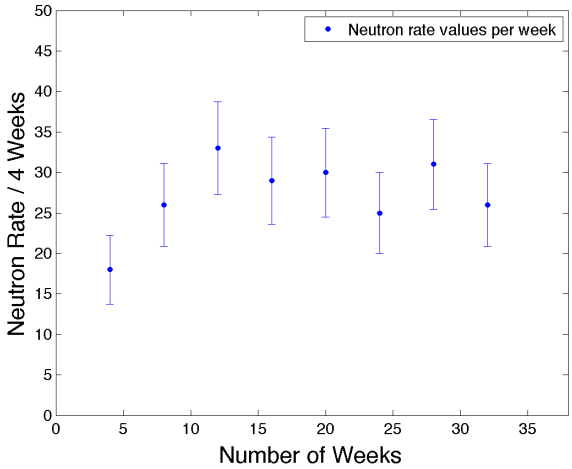
Neutron rate values per week
Neutron Rate / 4 Weeks
Number of Weeks

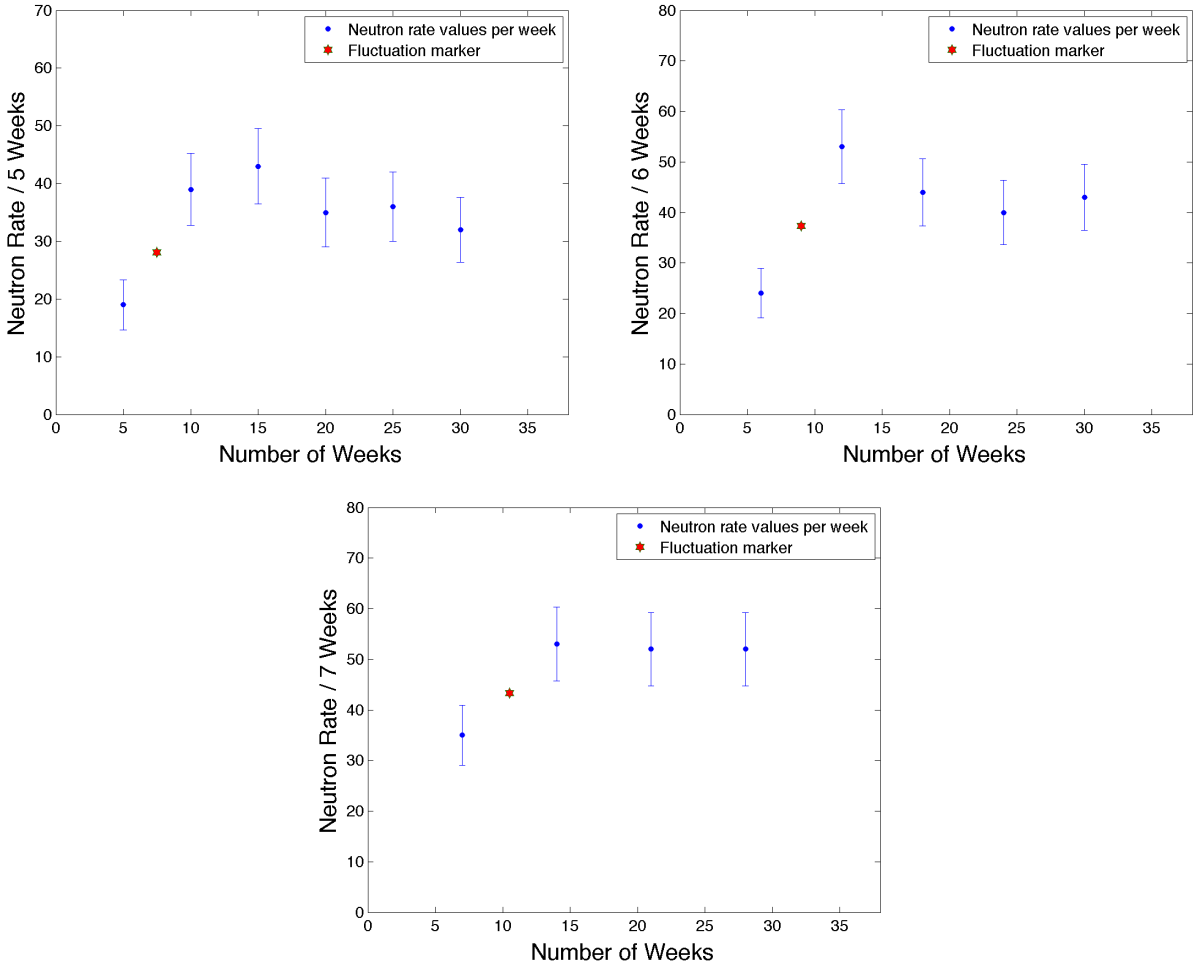

Figure 4.4: The measured neutron rates for a binning (time interval) of 1 until 7 weeks as addendum to Tab.4.3 and illustrated by plots. The fluctuations between 2 rate values, i.e. the non overlap of two subsequent statistical 1σ-errors of two neutron rate values, are indicated by a star marker placed between the corresponding 2 values. One or several fluctuations of the measured neutron rates are observed, for the time interval of 1 week in a) basically 3 times 3 subsequent fluctuations every 6 or 7 weeks within the available data of 34 weeks. However the rate value does not increase or decrease significantly, but it remains at the same level before and after the fluctuation in a), b) and c). In d), e), f) and g) no or only one fluctuation is visible. Due to the few available neutron rate data for large binnings in d), e), f) and g), a statement, whether the fluctuation observed is insignificant or not, can not be given. A significant fluctuation, i.e. a fluctuation over time intervals of months by in- or decreasing the rate value level significantly, is therefore not yet visible.

4.4 Outlook

As the time passes, the continuous data taking of the system will provide more measurement data than the current 34 weeks. A fluctuation in time intervals of the order of months might become observable then. If no fluctuation is observed, the neutron flux is indeed constant within the reach of the setup. To achieve more efficiency, improvement potential exists in several sections.

- A simple method to increase the efficiency is to use a larger LiI(Eu) crystal. Since its crytal and PMT have typical sizes, several similar LiI(Eu) detectors can be combined together.
- By choosing a LiI(Eu) detector crystal made of more radiopure material, less intrinsic α-background can be achieved which increases the neutron detection efficiency (see [23]).
- The neutron flux underground at LNGS might be different at the location of XENON100 than the ones obtained in [13]. Measurements or Monte Carlo simulations for the neutron flux and rate explicitly for that location will provide a more specific comparison with the measured ones of this experiment. However a rough measurement already exists which is in agreement with the calculated neutron flux of this experiment [24].

The most convenient method to improve the detection system might be by performing Monte Carlo simulations for the detection processes using the detector geometry. These simulations can be used to calculate the inefficiencies of the detection system and thus allows for their correction to obtain the absolute neutron flux. This method also gives evidence that the neutron the detector is understood.

References

[1] *http://map.gsfc.nasa.gov*

[2] *http://lambda.gsfc.nasa.gov*

[3] *http://lambda.gsfc.nasa.gov/produt/map/current/map_bibliography.com*

[4] K. Nakaura et al (Particle Data Group),
2010 Review of Particle Physics,
J. Phys G 37 (2010) 075021

[5] E. Aprile et al. (XENON Collaboration),
The XENON Dark Matter Experiment,
Astropart. Phys. 35, 573 (2012),
arXiv:1107.2155v1 [astro-ph.IM] (2011)

[6] *http://www.lngs.infn.it*

[7] http://www.physik.uzh.ch/groups/groupbaudis/darkmatter/grouptalks/
Marrodan_Xenon2010_CERN.pdf

[8] R. Caldwell, M. Kamionkowski,
Cosmology: Dark Matter and Dark Energy,
Nature 458, 587-589 (2 April 2009)

[9] R. Bernabei et al.,
New Results from DAMA/LIBRA,
arXiv:1002.1028v1 [astro-ph.GA] (Feb 2010)

[10] W. R. Leo,
Techniques for Nuclear and Particle Physics Experiments; A How-to Approach,
2nd Revised Edition, Springer-Verlag, Berlin-Heidelberg-New York, 1994

[11] R.B Firestone et al., *The Berkeley Laboratory Isotopes Project*,
URL: http://ie.lbl.gov/education/isotopes.htm

[12] Eckert & Ziegler AG, *Isotope Products*,
URL 1: http://www.ezag.com/de/startseite/produkte/isotope-products/industrial-sources.html,
URL 2: http://www.ezag.com/fileadmin/ezag/user-uploads/isotopes/isotopes/5_industrial_sources.pdf

[13] H. Wulandari et al.,
Neutron Flux at the Gran Sasso Underground Laboratory Revisited,
Astropart. Phys. 22 (2004) 313

[14] A. J. Deruytter, P. Pelfer,
Precise Determination of the Branching Ratio and Q-Value of the $^{1}0B(n,\alpha)^{7}Li$ *Reaction and of the Q-Value of the* $^{6}Li(n,\alpha)^{3}H$ *Reaction*,
Journal of Nuclear Energy, Vol. 21, Issue 11, Nov. 1967, Pages 833-845

[15] F. Gabbard, R. H. Davis, T. W. Bonner,
Study of the Neutron Reactions $^{6}Li(n,\alpha)^{3}H$, $^{19}F(n,\alpha)^{20}F$, $^{127}I(n,\gamma)^{128}I$,
Phys. Review, Vol. 114, Number 1, April 1959, The Rice Institute, Houston, Texas

[16] A. Syntfeld, M. Moszyński, R. Arlt, M. Balcerzyk, M. Kapusta, M. Majorov, R. Marcinkowski, P. Schotanus, M. Swoboda, D. Wolski,
^{6}*LiI(Eu) in Neutron and* γ*-ray Spectrometry - a highly sensitive thermal Neutron Detector*,
IEEE Transactions on Nuclear Science, Vol. 52, No. 6, December 2005

[17] G. Pausch, J. Stein,
Application of ^{6}*LiI(Eu) Scintillators with Photodiode Readout for Neutron Counting in Mixed Gamma-Neutron Fields*,
IEEE Transactions on Nuclear Science, Vol. 55, No. 3, June 2008

[18] *http://www.scionix.nl*

[19] *Scionix Datasheet of the High Voltage and amplification module AMP1000-HV-E3-X4*

[20] *Ortec Easy-MCA-8K Hardware User's Manual*

[21] *Ortec MAESTRO-32 A65-B32 Software User's Manual*

[22] *Scionix Testsheet of the LiI(Eu) Detector 25.4 B 3 / 1.5M - E1 - Li*

[23] M. Tarka,
Studies of Neutron Flux Suppression from a γ*-ray source and the GERDA Calibration System*,
PHD Thesis, Physics Institute of the University of Zurich, May 2012,
url: http://www.physik.uzh.ch/groups/groupbaudis/temp/PHD_Tarka/PHD_Tarka.pdf

[24] M. Haffke, L. Baudis, T. Bruch, A. Ferella, T. M. Undagoitia, M. Schumann, Y. Te, A. van der Schaaf,
Background Measurements in the Gran Sasso Underground Laboratory,
Nucl. Instr. Meth. A 643, 36 (2011), arXiv:1101.5298

5 Appendix: Particle Interactions in Matter

This chapter refers to chapter 1 and 2 of [10]. It contains basic knowledge of particle sources and interactions related to the experiment to a wider extent and in more detail than presented in chapter 2.

5.1 Production of γ-Radiation

The nucleus is characterized by discrete energy levels similar to the ones in atoms due to the electron shell structure. Between these levels transitions can be made in which electromagnetic radiation of a certain energy is emitted or absorbed. That energy is equal to the energy difference between the energy levels which participate in the transition. The binding energy of nuclei is much higher than that of electrons leading to higher photon energies ranging from a few hundred keV to a few MeV. These high energy photons were historically named γ-rays. As atoms they are characteristic for the emitting nucleus.

Most γ-sources end up in their exited states as the result of an α- or β-disintegration or are created in nuclear reactions [1]:

$$\alpha\text{-decay: } (Z,A) \rightarrow (Z-2, A-4) + \alpha \tag{5.1}$$

$$\begin{aligned} \beta^+\text{-decay: } (Z,A) &\rightarrow (Z-1,A) + e^+ + \nu_e \\ \text{resp. } p &\rightarrow n + e^+ + \nu_e \end{aligned} \tag{5.2}$$

$$\begin{aligned} \beta^-\text{-decay: } (Z,A) &\rightarrow (Z+1,A) + e^- + \bar{\nu}_e \\ \text{resp. } n &\rightarrow p + e^- + \bar{\nu}_e \end{aligned} \tag{5.3}$$

$$\begin{aligned} \text{Nuclear Reaction: } x + (Z,A) &\rightarrow (Z',A') + y \\ \text{resp. } I(x,y)J & \end{aligned} \tag{5.4}$$

where
- Z, Z' : Atomic number
- A, A' : Atomic mass number, i.e. sum of protons and neutrons
- x : One or several bombarding particles
- y : One or several outgoing particles
- I : Target nucleus
- J : Resulting nucleus

As an alternative to the β^+-decay, proton rich nuclei may also transform themselves via the capture of an electron from one of the atomic orbitals:

$$\text{Electron capture: } e^- + p \rightarrow n + \nu_e \tag{5.5}$$

[1] A common method for denoting nuclear reactions is A(x,y)B where x is the bombarding particle, A the target nucleus, B the resulting nucleus and y the outgoing particle(s). Thus the abbreviation (x,y) indicates any nuclear reaction in which x is the incident and y the outgoing particle.

The de-excitation of those states leads to the emission of γ-radiation.

The lifetime of these states is generally very short, i.e. the transition to a lower state occurs typically within 10^{-8} s. However there are states which may live much longer, so-called metastable states. Their de-excitation is usually hindered by a large spin difference between nuclear states.

The annihilation of positrons is another source of γ-rays. If a positron source such as ^{22}Na is encapsulated or allowed to irradiate an absorber material the positrons will annihilate with the absorber electrons producing two γ's each with an energy equal to the electron mass of 511 keV. Due to momentum conservation these two γ's are always emitted in opposite directions. Thus often only one of the two γ's is detected in a detector.

For the calibration measurements of the experiment (see chapter 3.1) the γ-sources ^{22}Na, ^{57}Co and ^{137}Cs were used. Their nuclear level diagrams are shown in Fig.5.1a, b and c. Every main decay emitting a γ in Fig.5.1, i.e. the β^+ and γ in a, the γ_2 in b as well as the γ in c, is observed as a peak in Fig.5.2. Thereby the correlation between γ-emission energy and peak in a corresponding measured source spectrum becomes possible as shown in Fig.5.2 which is necessary for the calibration in chapter 3.1. The spectra are measured with the γ-sensitive LiI(Eu) detector and associated electronics using the setup described chapter 3.3.1. The measurement time was 900 s real time (see chapter 3.2.3).

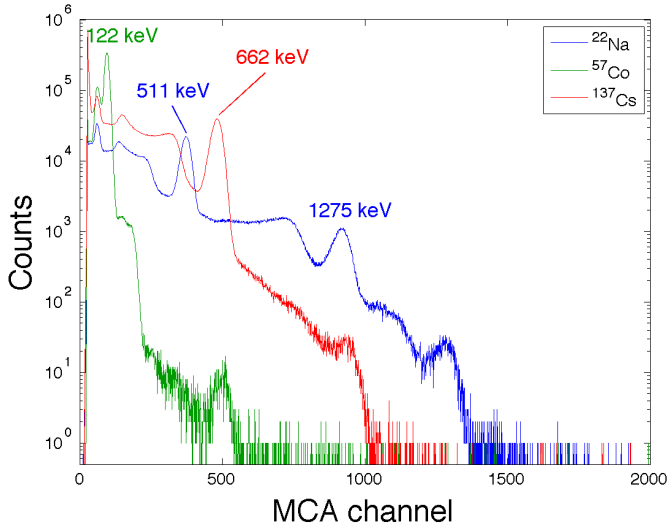

Figure 5.2: Measured γ-spectra of ^{22}Na, ^{57}Co and ^{137}Cs with the LiI(Eu) detector and associated electronics using the setup in chapter 3.3.1. Due to the positron annihilation in the detector and the ^{22}Na source itself, a peak at 511 keV is observed corresponding to one of the annihilation photons. Moreover three peaks are observed at 1275 keV, 662 keV and 122 keV in the corresponding spectra due to the absorption of photons emitted by the three sources.

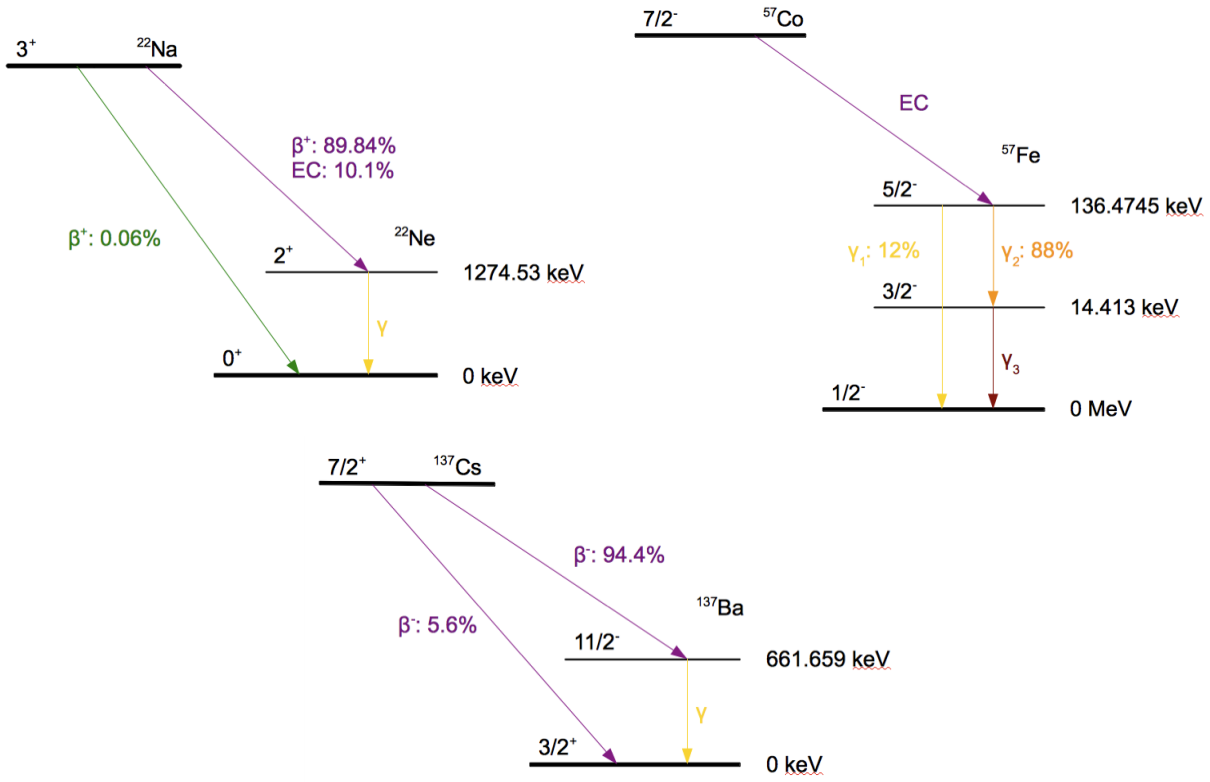

Figure 5.1: Nuclear level diagrams of ^{22}Na (a), ^{57}Co (b) and ^{137}Cs (c) [11]. The β^+-decay of ^{22}Na causes the emission of a positron annihilating with an atomic electron to produce two γ's each with an energy of 511 keV.

5.2 Interaction of γ-radiation

The photon can not perform inelastic collisions with atomic electrons due to the absence of its electric charge. Instead the main interactions of photons, in particular X- and γ-rays, are:

1. **Photoelectric Effect**
   It involves the absorption of a photon by an atomic electron with the subsequent ejection of the electron from the atom. The energy of the outgoing electron is

   $$E = h\nu - E_B, \tag{5.5}$$

   where E_B is the binding energy of the electron. The minimal energy threshold for this process to occur is thus E_B. Momentum conservation prohibits the absorption of a photon by a free electron and therefore requires that the photoelectric effect occurs on bound electrons where the nucleus absorbs the recoil momentum.

   As shown in Fig.5.3 which shows a typical cross section as a function of incident photon energy, the cross section is relatively small at energies above the highest

electron binding energy of the atom (the K-shell) but increases rapidly as the K-shell energy approaches. Since the K-shell electrons are no longer available for the photoelectric effect, the cross section drops drastically after this point. This rising and dropping continues for all further shells like L, M, etc. The photoelectric effect is difficult to treat in theory rigorously but it can be calculated easier assuming photon energies above the K-shell and not too relativistic energies, i.e. $E \lesssim m_e = 0.511$ MeV. In this case it behaves like

$$\sigma \sim \text{const.} \cdot \frac{Z^n}{E_\gamma^{3.5}}, \tag{5.6}$$

where Z is the atomic number and n is between 4 and 5 for MeV γ-energies.

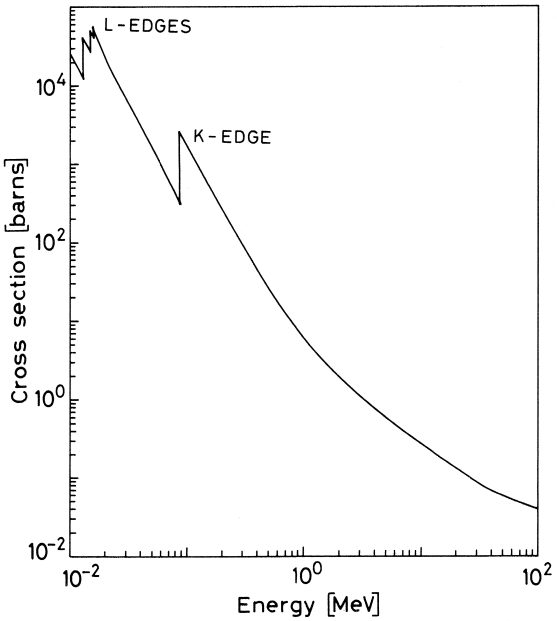

Figure 5.3: Example of a photoelectric cross section calculated for lead.

2. **Compton Scattering**
This process describes the scattering of photons on free electrons. In matter electrons are bound. However, if the photon energy is high enough with respect to the binding energy of the electron, the latter energy can be neglected and the electrons can be considered as free. Applying energy and momentum conservation one can obtain the following equations:

$$\frac{1}{E'_\gamma} - \frac{1}{E_\gamma} = \frac{1}{m_e c^2}(1 - \cos(\theta)) \tag{5.7}$$

The energy transfer onto the scattered photon is thus

$$E'_\gamma = \frac{E_\gamma}{1 + \frac{E_\gamma}{m_e c^2}(1 - \cos(\theta))} \tag{5.8}$$

and the one onto the scattered electron

$$E_{e^-} = E_\gamma - E'_\gamma = E_\gamma \frac{\frac{E_\gamma}{m_e c^2}(1-\cos(\theta))}{1+\frac{E_\gamma}{m_e c^2}(1-\cos(\theta))}, \tag{5.9}$$

where θ is the scattering angle, E_γ the initial photon energy and m_e the electron mass. In the case of back scattering ($\theta = \pi$) the energy transfer to the electron is maximal (see eq.(5.12)).

The cross section for Compton scattering can be calculated using quantum electrodynamics. In the limit case $E_\gamma \gg m_e c^2$ the complex formula can be simplified to:

$$\sigma = \pi \frac{\alpha^2 c^2}{m_e E_\gamma} \left(\frac{1}{2} + \ln\left(\frac{2E_\gamma}{m_e c^2} \right) \right), \tag{5.10}$$

and for Z electrons:

$$\sigma \sim \frac{Z}{E_\gamma} \tag{5.11}$$

where $\alpha \simeq \frac{1}{137}$ Fine structure constant
m_e : Electron mass
E_γ : γ-energy
c : Speed of light

which holds roughly for γ-rays in the MeV region. Fig.5.4a shows the Compton cross section as a function of the photon energy.

The energy distribution shown in Fig.5.4b of the recoil electrons can be obtained from eq.(5.9). The maximum recoil energy allowed by kinematics is referred to as the Compton edge

$$E_{\max} = \frac{2E_\gamma^2}{m_e c^2 + 2E_\gamma}. \tag{5.12}$$

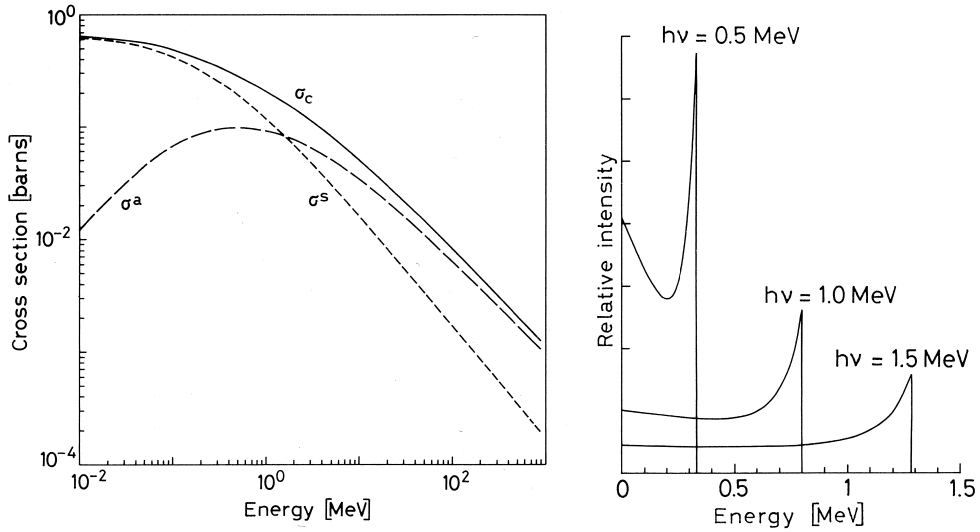

Figure 5.4: a) Compton scattered cross section σ^s, compton absorption cross section σ^a and their sum $\sigma_c = \sigma^s + \sigma^a$. σ^s corresponds to the average fraction of the total energy contained in the scattered photon while σ^a corresponds to the average energy transferred to the recoil electron which is stopped in the material and its energy fraction thus absorbed by the material.
b) Energy distribution of the compton recoil electrons. The sharp drop at the maximum recoil energy is known as the Compton edge. In experimental measurements of γ-sources as in Fig.5.2 the peak is much wider due to the finite energy resolution and is closely followed by a photon- or positron annihilation peak resulting in a less steeper drop.

3. **Pair Production**
This process describes the transformation of a photon into an electron-positron pair. Due to momentum conservation, this occurs only in the presence of a third body, usually a nucleus. Furthermore the photon must have at least an energy of 1.022 MeV to create a pair. Due to the momentum transfer to the nucleus there is actually a little bit more energy required:

$$E_\gamma \geq 2m_e c^2 + \underbrace{2\frac{m_e^2}{M}c^2}_{\substack{\text{generally} \\ \text{negligible} \\ \text{small}}} \geq 1.022 \text{ MeV} \tag{5.13}$$

The screening by the atomic electrons surrounding the nucleus plays an important role and is a reason why the calculation of pair production cross sections is complicated. To obtain it, a numerical integration of the differential cross section must generally be performed. In the limit cases of no screening and complete screening an

analytical integration is possible leading to:

$$\begin{aligned} &\text{No screening: } m_e c^2 \ll E_\gamma \ll \frac{1}{\alpha} m_e c^2 Z^{-1/3} \\ &\sigma = 4\frac{\alpha^3 Z^2}{m_e^2}\left\{\frac{7}{9}\left[\ln\left(\frac{2E_\gamma}{m_e c^2}\right) - f(Z)\right] - \frac{109}{54}\right\} \sim Z^2 \ln(E_\gamma) \end{aligned} \tag{5.14}$$

$$\begin{aligned} &\text{Complete screening: } E_\gamma \gg \frac{1}{\alpha} m_e c^2 Z^{-1/3} \\ &\sigma = 4\frac{\alpha^3 Z^2}{m_e^2}\left\{\frac{7}{9}\left[\ln\left(\frac{183}{Z^{1/3}}\right) - f(Z)\right] - \frac{1}{54}\right\} \sim Z^2 \text{ const.} \\ &\text{where } f(Z) \simeq Z^2\alpha^2\left(\frac{1}{1+Z^2\alpha^2} + 0.2026\right). \end{aligned} \tag{5.15}$$

f(Z) is a small correction which takes the Coulomb interaction of the electron or positron in the electric field of the nucleus into account. Fig5.5 illustrates the energy dependence of the total pair production the cross section.

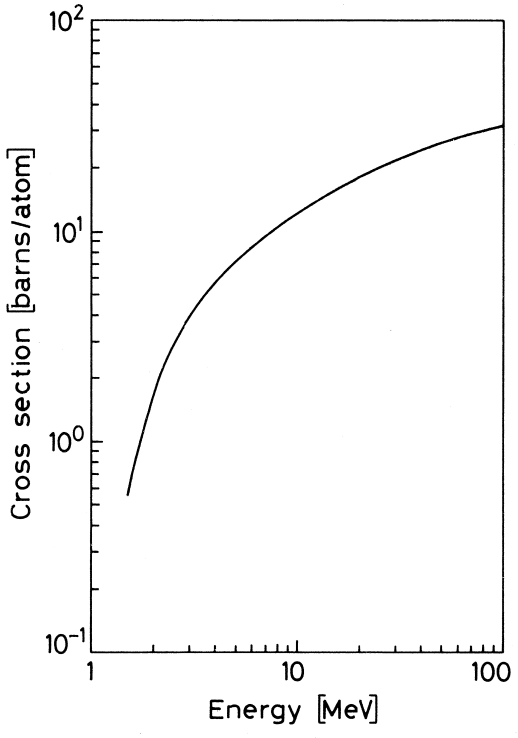

Figure 5.5: Pair production cross section in lead.

Pair production may also occur in the field of an atomic electron which leads to a similar result for the cross section but smaller by about a factor of Z. One only needs

to replace Z^2 by $Z(Z+1)$ in the above formulae to approximately account for this interaction.

The 3 main reactions explain two principal qualitative feature of γ-rays:

1. They are more penetrating in matter than stable charged particles since the cross-section of the 3 processes are much smaller relative to the elastic resp. inelastic electron collision cross-section.

2. A beam of photons passing through a thickness of matter is only weakened in its intensity not in its energy since the three processes above remove the photon completely from the beam, either by absorption or scattering.

5.3 Production of Neutrons

Commercially available neutron sources, as used in this experiment for calibration purposes, are either based on spontaneous fission or a nuclear reaction. Natural neutron emitters which can be used practically in the lab do not exist. They have to be produced synthetically. The more convenient method of producing neutrons is with the nuclear reactions (α, n) or (γ, n).

For the calibration of this experiment (see chapter 3.3.2), a ^{241}Am^{9}Be neutron source is used. Such a source is generally made by mixing the target material ^{9}Be with a suitably strong α- or γ-emitter. In this case the α-emitter ^{241}Am is fixed onto one flat side of the cylindrical ^{9}Be target [**?**]. Under α bombardment ^{9}Be undergoes the following reactions which lead to the production of free neutrons:

$$\alpha \; + \; {}^{9}Be \; \longrightarrow \; {}^{13}C^{(*)} \; \longrightarrow \; \begin{cases} {}^{12}C^{(*)} \; + \; n \\ {}^{8}Be \; + \; \alpha \; + \; n \, . \\ 3\alpha \; + \; n \end{cases} \tag{5.16}$$

The dominant reaction is the decay from ^{13}C to ^{12}C or to the 4.44 MeV excited state of ^{12}C which is denoted by $^{(*)}$. A neutron yield of about 70 n's per 10^6 α's is obtained if ^{241}Am is the α-source. The α-emitter's half-life and activity determines therefore the half-life and activity of the neutron production.

For incident α's of a fixed energy the energy spectrum of the emitted neutrons should theoretically show monoenergetic lines corresponding to the different transitions which are made. In mixed sources such as AmBe however there is a smearing of the α-particle spectrum due to the energy loss between origin and capture of the α-particle inside the source and target material itself such that a large smearing in neutron energy results. This is illustrated in Fig.5.6b.

If ^{241}Am decays by emitting an α-particle into ^{237}Np, this daughter nucleus offers many possibilities of excited states whose de-excitation into the ground state results in the emission of γ-particles. The nuclear level diagram of ^{241}Am is therefore quite complex and it

makes sense to simplify it by taking into account only branching ratios larger than 0.3% shown in Fig.5.6a.

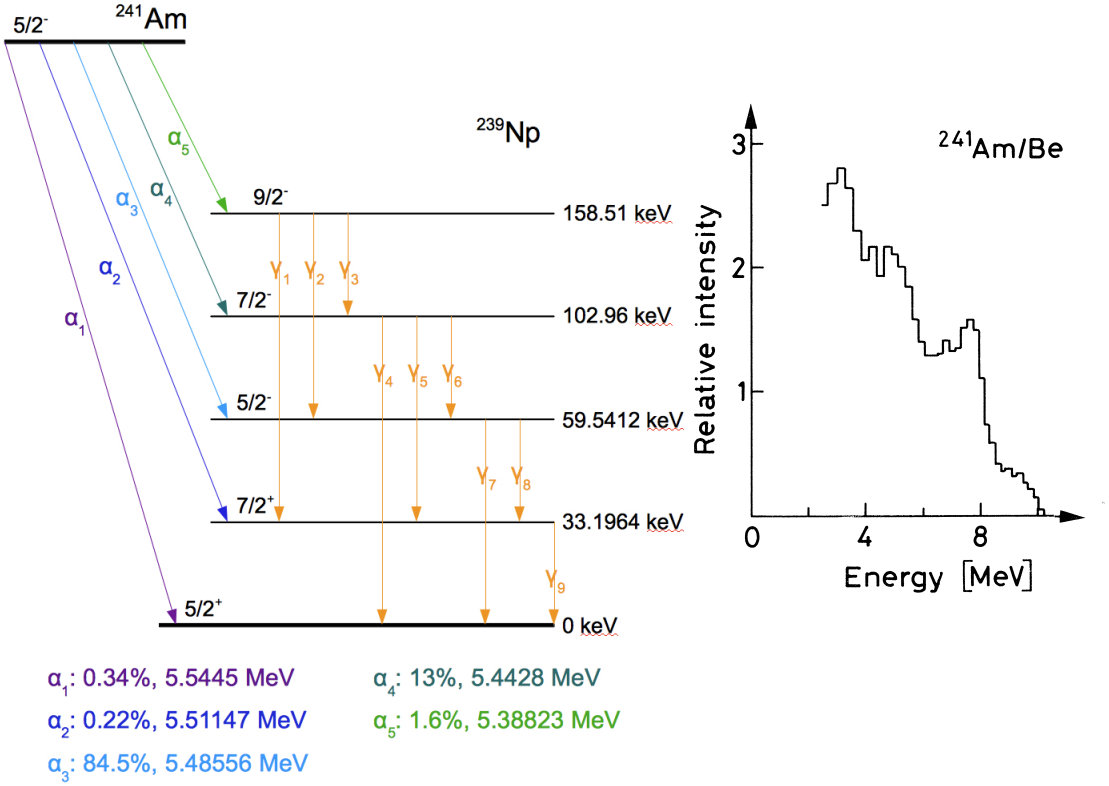

Figure 5.6: a) Nuclear level diagram of ^{241}Am restricting the α-decay possibilities to branching ratios larger than 0.3% [11].
b) Neutron energy spectrum from ^{241}Am^{9}Be.

5.4 Interactions of Neutrons; Moderation and Capture

As the photon the neutron does not possess an electric charge. It is not subject to electromagnetic interactions with the electrons and nuclei in matter. Instead, its principal way of interaction is through the strong force with nuclei whereat the interaction probability is much rarer compared to the one of electrons for instance due to the short range of this force. A neutron must come within $\simeq$ 1 fm of the nucleus before an interaction can take place. Since baryonic matter is mainly "empty space" the neutron is a very penetrating particle, much more than γ-rays. When a neutron interacts it may undergo a variety of nuclear processes depending on its energy:

1. a) Elastic scattering from nuclei, i.e. $A(n,n)A$.
   This process is the principal mechanism of energy loss of neutrons with energies of about a few MeV.

   b) Inelastic scattering, e.g. $A(n,n')A^{(*)}$, $A(n,2n')B$, etc.
   After such reactions the nucleus is left in an excited state which might later decay via another form of radiative emission like γ-rays. The neutron must have sufficient energy to excite the nucleus, usually of the order of 1 MeV or more, for the inelastic reaction to occur. Below this threshold only elastic scattering occurs.

2. a) Radiative neutron capture, i.e. $n + (Z,A) \rightarrow \gamma + (Z, A+1)$.
   In general the cross section for neutron capture goes like

$$\sigma \simeq \frac{1}{v}, \tag{5.17}$$

   where v is the velocity of the neutron. The capture is therefore most likely at low energies. Resonance peaks superimposed upon this dependence may also be present depending on the element. At these energies the capture probability is greatly enhanced.

   b) Other nuclear reactions such as (n,p), (n,d) [3], (n,α), (n,t) [4], $(n,\alpha{+}p)$, in which the neutron is captured and charged particles are emitted. These reactions occur generally in the eV to keV region. The capture cross section and resoncances follow the same behaviour as for radiative neutron capture.

   c) Fission, i.e. (n,f) [5], which again is most likely at low energies.

3. High-energy hadron shower production which occurs only for very high-energy neutrons with $E_n > 100$ MeV.

Neutrons are classified according to their energy since their interactions depend strongly on their energy although no strict boundaries exist among the classes. High energy neutrons have energies above $E_n \simeq 100$ MeV, those between a few ten's of MeV and a few hundred keV are known as fast neutrons. Between $E_n \simeq 100$ keV and $E_n \simeq 0.1$ eV, where nuclear resonance reactions occur, neutrons are referred to as epithermal, whereas at lower energies comparable to the thermal energy at room temperature, i.e.
$E_n \simeq kT \simeq 1/40$ eV $= 25$ meV, neutrons are called thermal. Moreover for energies lower than the thermal neutrons are referred to as cold where $E_n \lesssim 2$ meV and below as ultracold where $E_n \lesssim 0.2$ meV.

The total probability for a neutron to interact with matter is given by the sum of the individual cross sections:

$$\sigma_{\text{tot}} = \sigma_{\text{elastic}} + \sigma_{\text{inelastic}} + \sigma_{\text{capture}} + ... \tag{5.18}$$

[3] d denotes deuterium which is the isotope ${}^2_1\text{H}$ (without electrons)
[4] t denotes tritium, the isotope ${}^3_1\text{H}$
[5] f denotes one ore more decay nuclei along with one or more neutrons

The slowing down of neutrons by interaction in matter is called as moderation. If a fast neutron enters into matter it will scatter back and forth on the nuclei, elastically and inelastically. It loses energy until it comes into thermal equilibrium with the surrounding atoms. At this point it will diffuse through matter until it is finally captured by a nucleus and undergoes one of the processes mentioned above (2.a), b), c)). The neutron may also undergo a nuclear reaction or be captured before attaining thermal energies, especially if resonances are present. However the energy dependence of the cross-section in eq.(5.17) favors the survival of the neutrons down to thermal energies.

Elastic scattering (1.a)) is the principal mechanism of energy loss for fast neutrons. At energies of several MeV, which is the case in this experiment, the problem can be treated nonrelativistically with conservation laws. Consider a single collision in the lab frame of reference between a neutron with velocity of v_0 and a nucleus at rest with a mass M as shown in Fig.5.7.

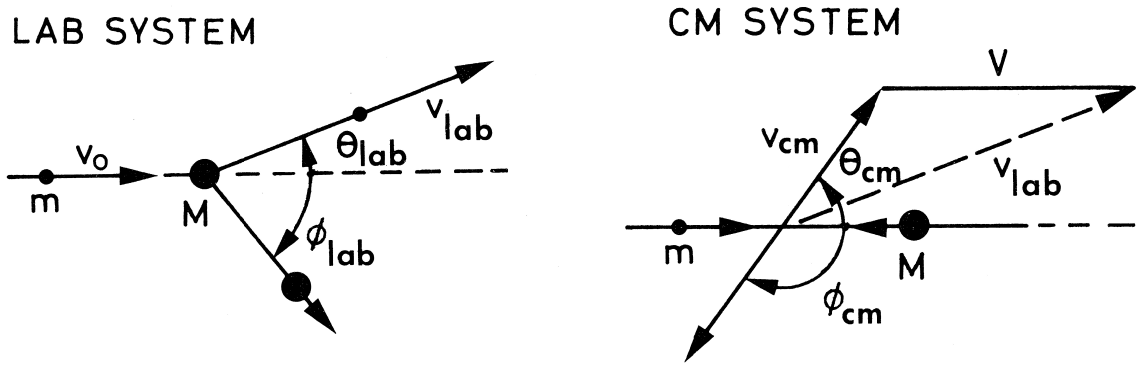

Figure 5.7: Elastic scattering of a neutron on a nucleus of mass M in the lab- (a) and center of mass (cm) frame (b).

Energy and momentum conservation for the lab system require:

$$\underbrace{\overrightarrow{p}_{\text{nucl.}}}_{=0} + \overrightarrow{p}_{\text{neutr.}} = \overrightarrow{p}'_{\text{nucl.}} + \overrightarrow{p}'_{\text{neutr.}}, \tag{5.19}$$

whereas in the center of mass (cm) system:

$$\overrightarrow{p}_{\text{nucl.}} = \overrightarrow{p}_{\text{neutr.}} \quad . \tag{5.20}$$

Setting the neutron mass $m_n = 1$ (and neglect the neutron and proton mass difference) the mass of the nucleus is the atomic mass number A. Transforming to the center of mass (cm) system and deriving the recoil energy of the nucleus and the energy of the scattered neutron we get:

$$E'_{\text{nucl.}} = E_{\text{neutr.}} \frac{4A}{(A+1)^2} \cos^2(\phi_{\text{lab}}) = E_{\text{neutr.}} \frac{2A}{(A+1)^2}(1 + \cos(\phi_{\text{cm}})), \tag{5.21}$$

$$E'_{\text{neutr.}} = E_{\text{neutr.}} \frac{\left(\cos(\theta_{\text{lab}})) + \sqrt{A^2 - \sin^2(\theta_{\text{lab}})}\right)^2}{(A+1)^2} = E_{\text{neutr.}} \frac{A^2 + 1 + 2A\cos(\theta_{\text{cm}})}{(A+1)^2}. \quad (5.22)$$

From eq.(5.22) we see that the scattered neutron is limited to the range

$$\left(\frac{A-1}{A+1}\right)^2 E_{\text{neutr.}} < E'_{\text{neutr.}} < E_{\text{neutr.}} \quad (5.23)$$

where the limits correspond to $\cos(\theta_{cm}) = \pm 1$. In the case of scattering at protons, $A = 1$ and

$$0 < E'_{\text{neutr.}} < E_{\text{neutr.}}. \quad (5.24)$$

This implies that the slowing down of neutrons is most efficient when protons or light nuclei are used. This is not surprising since intuitively, the lighter the nucleus, i.e. the smaller the mass difference between neutron and target particle is, the more recoil energy it absorbs from the neutron. This explains the use of hydrogenous materials such as water (H_2O), paraffin ($(CH_2)_n$) and polyethylene (C_2H_{4n}) for neutron moderation.

The energy distribution of the scattered neutron at not too high energies, i.e. $E_{\text{neutr.}} \leq 15$ MeV, is given by the differential probability density function:

$$\frac{dw_1}{dE} = \frac{1}{E_{\text{neutr.}}} \frac{(A+1)^2}{4A} = \frac{1}{E_{\text{neutr.}} \left(1 - \left(\frac{A-1}{A+1}\right)^2\right)} \quad . \quad (5.25)$$

Therefore the energy distribution of an originally monoenergetic neutron is constant over the energy range after one scattering. This result helps to find the distribution after two scatterings:

$$\frac{dw_2}{dE} = \begin{cases} \displaystyle\int_{E'_{\text{neutr.}}}^{E_{\text{neutr.}}} d\epsilon \frac{dw_1}{d\epsilon} \frac{1}{\epsilon(1-\eta)} = \frac{1}{E_{\text{neutr.}}(1-\eta)} \ln\left(\frac{E_{\text{neutr.}}}{E'_{\text{neutr.}}}\right) \ , \ \eta E_{\text{neutr.}} < E'_{\text{neutr.}} < E_{\text{neutr.}} \\ \displaystyle\int_{\eta E_{\text{neutr.}}}^{E'_{\text{neutr.}}/\eta} d\epsilon \frac{dw_1}{d\epsilon} \frac{1}{\epsilon(1-\eta)^2} = -\frac{1}{E_{\text{neutr.}}(1-\eta)^2} \left(\ln\left(\frac{E_{\text{neutr.}}}{E}\right) + 2\ln(\eta)\right), \\ \eta^2 E_{\text{neutr.}} < E'_{\text{neutr.}} < \eta E_{\text{neutr.}} \end{cases} \quad (5.26)$$

where $\eta = \left(\frac{A-1}{A+1}\right)^2$.

For more scatterings the distribution can be calculated but the algebra becomes more and more complicated. In the more general case of n scatterings on hydrogen the distribution formula is:

$$\frac{dw_n}{dE} = \frac{1}{E_{\text{neutr.}}(n-1)!} \left[\ln\left(\frac{E_{\text{neutr.}}}{E'_{\text{neutr.}}}\right)\right]^{n-1} \quad . \quad (5.27)$$

Fig.5.8 compares those calculated distributions after one resp. several scatterings.

This treatment illustrates the complexity of energy information of neutrons during scattering, since the calculation is restricted to an upper limit on the incident neutron energy as well as to the approach of s-wave scattering. Moreover an exact result would need the number of scatterings which is in general highly material dependent and only calculable as an average due to the statistical distributed variation in the path lengths between the scatterings.

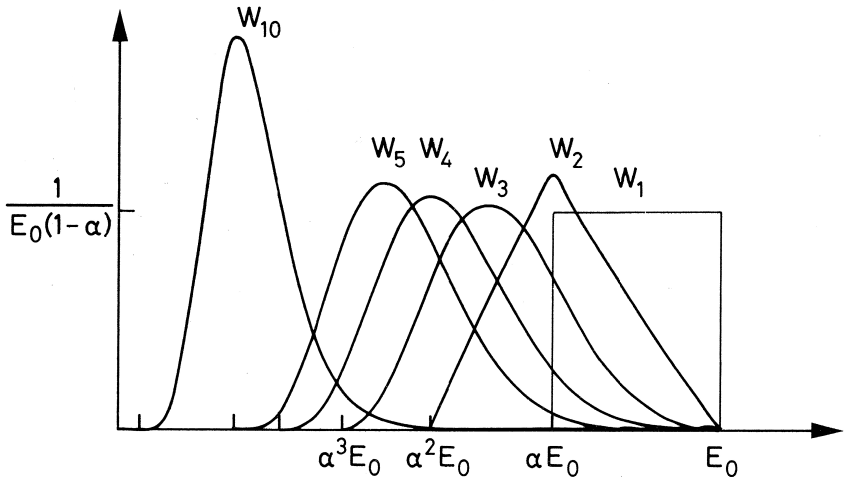

Figure 5.8: Energy distribution of neutrons after one resp. several elastic scatterings. I.e. it shows the probability density function w versus the neutron energy $E_{\text{neutr.}}$ within the boundaries $0 < E'_{\text{neutr.}} < E_{\text{neutr.}}$ developing with the number of elastic scatterings where $\alpha = \left(\frac{A-1}{A+1}\right)^2$.

5.5 Energy Loss of Heavy Charged Particles by Atomic Collisions

In general the passage of charged particles through matter is characterized by two features: The particle loses energy and it is deflected from its incident direction. These effects are primarily the cumulative result of two processes which occur many times per unit path length in matter:

1. Inelastic collisions with the atomic electrons of the material
2. Elastic scattering from nuclei

However these are not the only reactions which can occur. Other processes include:

3. Emission of Cherenkov radiation
4. Nuclear reactions
5. Bremsstrahlung

For kinetic particle energies $E \lesssim 100$ MeV they are extremely rare compared to the atomic collision processes and thus will be ignored here. Since the mass of the electron is much smaller compared to a proton, it is customary to separate charged particles into two classes: a) Electron and positrons and b) heavy particles, i.e. particles heavier than the electron. The focus of this chapter is on this latter class which includes muons, pions, protons, α particles and other light nuclei [6].

Of the two listed electromagnetic processes 1. and 2., the inelastic collisions are almost solely responsible for the energy loss of heavy particles in matter, typical cross sections are $\sigma \simeq 10^7 - 10^8$ b. In this process energy is transferred from the particle to the atomic electron resulting in an excitation or ionization of this electron. Indeed the amount of energy transferred in each collision is a very small fraction of the kinetic energy of the particle (a few eV). However in solid state bodies the number of collision electrons and thus the number of collisions per unit path length is so large that a significant cumulative energy loss is observed in relatively thin layers of material. An example: A 10 MeV proton loses all of its kinetic energy in 0.25 mm of copper.

Elastic scattering from nuclei also occurs frequently, although not as often as electron collisions. Also in this case very little energy is transferred since the masses of most nuclei are large compared to the incident particle. Exceptions are for example α-particles in hydrogen or α's in lithium where some energy is also lost through this mechanism. Nevertheless the major part of the energy loss is still due to atomic electron collisions which is the reason why only this process is considered from now on.

The inelastic collisions occur with a certain quantum mechanical probability and are statistical in nature. Because of their large number per macroscopic pathlength the fluctuations in the energy loss are small. Thus one can work with the average energy loss per unit path length, often called stopping power dE/dx.

We consider a hevy particle with charge $z \cdot e$, mass M and velocity v passing through some material. Suppose also an atomic electron being at some distance b from the particle trajectory (see Fig.5.9a). We assume further that the electron is free, initially at rest and that it only moves slightly during the interaction with the heavy particle such that the electrical field acting on the electron is considered at its initial position. After the collision the incident particle is assumed to be undeviated from its original path due to the much larger mass compared to the one of the electron. The formalism for gaining the energy lost to all the electrons between a distance b_{min} and b_{max} leads to (Bohr's classical formula)

[6] Particles heavier than these, i.e. the heavy ions have to be excluded because of additional arising effects.

$$-\frac{dE}{dx} = \frac{4\pi z^2 e^4}{m_e v^2}\rho_e \ln\left(\frac{b_{\max}}{b_{\min}}\right) = \frac{4\pi z^2 e^4}{m_e v^2}\rho_e \ln\left(\frac{\gamma^2 m_e v^3}{z e^2 \overline{\nu}}\right) \sim \frac{z^2}{v^2} \tag{5.28}$$

where $b_{min} = \dfrac{ze^2}{\gamma m_e v^2}$

$b_{max} = \dfrac{\gamma v}{\overline{\nu}}$

$\beta = \dfrac{v^2}{c^2}$

$\gamma = \dfrac{1}{\sqrt{1-\beta^2}}$

$\overline{\nu}$: A mean orbital frequency of the bound electrons averaged over all bound states

m_e : Electron mass

z : Charge of incident particle in units of e

e : Elementary charge

(5.29)

This formula gives a reasonable description of the energy loss for α-particles of heavier nuclei but for lighter particles, e.g. the proton, it breaks down due to quantum effects.

The correct quantum mechanical calculation yields the Bethe-Bloch formula:

$$-\frac{dE}{dx} = 2\pi N_a \rho \frac{e^4}{m_e c^2}\frac{Z}{A}\frac{z^2}{\beta^2}\left[\ln\left(\frac{2m_e\gamma^2 v^2 W_{max}}{I^2}\right) - 2\beta^2 - \delta - 2\frac{C}{Z}\right] \sim \frac{\rho Z z^2}{A\beta^2} \tag{5.30}$$

where $N_a = 6.022 \cdot 10^2 3 \text{ mol}^{-1}$ Avogadro's number

m_e : Electron mass

e : Elementary charge

$\beta = \dfrac{v^2}{c^2}$

$\gamma = \dfrac{1}{\sqrt{1-\beta^2}}$

I: Mean excitation potential

Z: Atomic number of absorbing material

z: Charge of incident particle in units of e

A: Atomic mass number

ρ: Density of absorbing material

δ: Density correction

C: Shell correction

W_{max}: Maximum energy transfer in a single collision

Fig.5.9b shows a plot of this formula as a function of kinetic energy of different particles. For non-relativistic energies dE/dx is dominated by the $1/\beta$ dependence and decreases with increasing velocity until $v \simeq 0.96c$, where the minimum is reached. This minimum is almost the same for particles with the same charge. As the velocity increases further $1/\beta$ becomes nearly constant and dE/dx rises due to the logarithmic dependence. Eq.(5.30) breaks down in the low energy region due to several arising complicating effects, e.g. the electron pick-up of the particle for short times which reduces its effective charge.

From Fig.5.9b one observes that as a heavy charged particle is slowed down in matter, its rate of energy loss will change as its kinetic energy changes. Indeed more energy per unit path length is deposited towards the end of its path due to the $1/\beta^2$ dependence in eq.(5.30) before at the very end of its trajectory it begins to pick up electrons and dE/dx drops. This behaviour is illustrated in Fig.5.10 which shows the amount of ionization created by a hevy charged particle as a function of its position along is slowing-down path and is known as a Bragg curve.

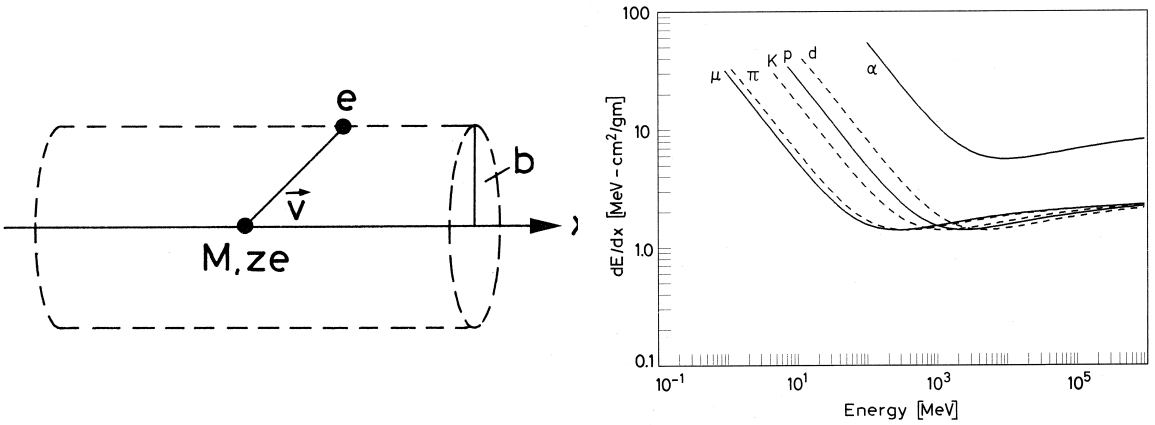

Figure 5.9: a) Collision of a hevy charged particle with an atomic electron.
b) The stopping power dE/dx as a function of energy for different incident particles.

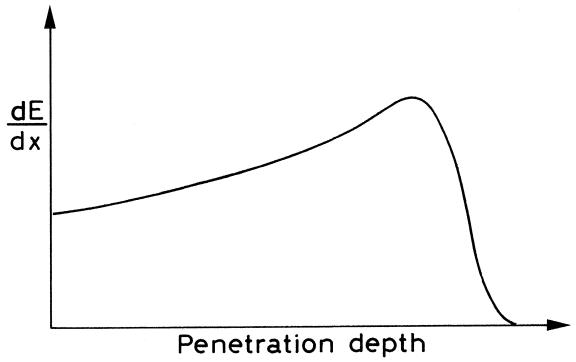

Figure 5.10: A typical Bragg curve showing the variation of dE/dx as a function of the penetration depth of the particle in matter. The particle deposits more energy towards the end of its path leading to the Bragg peak shortly before it is stopped.